Title

High-Temperature Thermal Diffusivity Measurements Using a Modified Ångström's Method With Transient Infrared Thermography

Journal

Journal of Heat Transfer, 144(2)

ISSN

0022-1481

Authors

Hu, Yuan
Abuseada, Mostafa
Alghfeli, Abdalla
et al.

Publication Date

2022-02-01

DOI

10.1115/1.4053108

Peer reviewed

High-temperature thermal diffusivity measurements using a modified Ångström's method with transient infrared thermography

Yuan Hu
Mechanical and Aerospace Engineering Department
University of California,
Los Angeles, CA 90095
Email: yuan.hu@ucla.edu

Mostafa Abuseada
Mechanical and Aerospace Engineering Department
University of California,
Los Angeles, CA 90095
Email: mabuseada@ucla.edu

Abdalla Alghfeli
Mechanical and Aerospace Engineering Department
University of California,
Los Angeles, CA 90095
Email: alghfeli@ucla.edu

Saurin Holdheim
Mechanical and Aerospace Engineering Department
University of California,
Los Angeles, CA 90095
Email: saurinholdheim@gmail.com

Timothy S. Fisher*
Mechanical and Aerospace Engineering Department
University of California,
Los Angeles, CA 90095
Email: tsfisher@ucla.edu

ABSTRACT

This work reports a method to measure thermal diffusivity of thin disk samples at high temperatures (approx. 900 - 1150 K) using a modified Ångström's method. Conventionally, samples are heated indirectly from the surroundings to reach high temperatures for such measurements, and this process is time-consuming, typically requiring hours to reach stable temperatures. In this work, samples are heated directly in a custom instrument by a concentrated light source and are able to reach high steady-periodic temperatures in approx. 10 min., thus enabling rapid thermal diffusivity characterization. Further, existing Ångström's methods for high temperature characterization use thermocouples for temperature detection that are commonly attached to samples via drilling and welding, which are destructive to samples and introduce thermal anomalies. We use an infrared camera calibrated to 2000 °C for non-contact, non-destructive and data-rich temperature measurements and present an image analysis approach to process the IR data that significantly reduces random noise in temperature measurements. We extract amplitude and phase from processed temperature profiles and demonstrate that these metrics are insensitive to uncertainty in emissivity. Previous studies commonly use regression approaches for parameter estimation that are ill-posed (i.e., non-unique solutions) and lack rigorous characterization of parameter uncertainties. Here, we employ a surrogate-accelerated Bayesian framework and a 'No-U-Turn' sampler for uncertainty quantification. The reported results are validated using graphite and copper disks and exhibit excellent agreement within 5% as compared to reference values obtained by other methods.

*Corresponding author.

1 Introduction

Accurate thermal diffusivity characterization at high temperatures is crucial in the aerospace and energy industries, among others. Currently, the laser-flash [1–5], transient plane source [6], hot wire [7] and Ångström's [8] [9] methods are commonly used for such characterization. Compared to other methods, Ångström's method is robust and simple to realize. Typically a portion of a sample is periodically heated, and thermal diffusivity is extracted by analyzing amplitude and phase differences between temperature profiles along the heat conduction direction. The method typically does not require knowledge or precise control of (1) contact resistance between the sample and the heater, (2) heat input to the sample, and (3) sample heat loss to the surroundings.

Ångström's method has been used for thermal diffusivity characterization at high temperatures in a relatively small number of previous studies that can be categorized into in-plane and cross-plane measurements. For in-plane measurements, a sample is typically circular in shape and heated to high temperatures by a furnace. Upon reaching steady temperatures, the curved outer surface is heated periodically by the furnace, whereas flat faces are often thermally insulated. Thermal waves are propagated along the radial direction, two thermocouples are placed at different radii to measure oscillatory temperature profiles, and thermal diffusivity is computed from temperature amplitude decay, phase shift, or both. Katsura [10] used such a technique on silica glass up to 9 GPa and 1200 K with approx. 3% accuracy. Xu et al. [11] used a similar apparatus and measured olivine, wadsleyite and ringwoodite up to 1373 K with 12% accuracy. For thin sheets or foils, Hatta et al. [12] used a mask to cover part of a strip sample and irradiated both the sample and the mask using a lamp with periodic intensity. Thermal diffusivity was calculated by measuring the decay of temperature oscillation at multiple locations within the masked region. This method achieved 5% accuracy for in-plane thermal diffusivity of nickel foil up to 500 °C.

For cross-plane measurements, a cylindrical sample can be periodically heated at either a top or bottom surface. Typically two or three thermocouples are placed at different axial locations to measure temperature oscillations, and thermal diffusivity is extracted based on amplitude decay and phase shift. Sidles and Danielson [9] developed an apparatus to measure copper and nickel rods (>50 cm) up to 500 °C. Abeles et al. [13] reported an apparatus that measures thermal diffusivity of short cylindrical solids (Armco iron and germanium) up to 1000 °C with an accuracy of approx. 2% using relatively high heating frequencies. Vandersande and Pohl [14] reported an instrument that is more convenient to assemble and is capable of measuring thermal diffusivity between 80-500 K with 3% to 7% accuracy. An alternative technique for cross-plane thermal diffusivity measurements was developed by Cowan [15]. The method is similar to laser flash and is suitable for electrically conductive thin disks. In Cowan's method, a high-intensity electron gun with uniform intensity distribution bombards the front side of the disk periodically. The temperature phase difference between the front and the back surfaces of the disk is used to determine thermal diffusivity. Wheeler [16] used this approach and measured refractory metals up to 3000 K with 5% accuracy. Tanaka and Suzuki [17] employed a similar technique on pyrolytic graphite up to 1900 K with 5% accuracy.

Most of the foregoing methods require a heat source external to the sample to heat it and the surroundings to high temperature prior to periodic heating. This process is typically lengthy, requiring hours to reach steady, elevated temperature. To mitigate heat loss, radiation shields are often used that preclude the use of non-contact, non-intrusive temperature detection. Thermocouples are commonly used, and drilling or welding is typically involved to attach thermocouples to the sample, introducing heat losses and potentially altering the sample's structure. In addition, temperature measurements are limited by the number of thermocouples, leading to unreliable results if defects are present between the thermocouples [18].

In this work and in contrast to methods that heat samples from surroundings, we employ a concentrated light source to directly heat samples (3.5" OD thin disks) to high temperatures to measure in-plane thermal diffusivity. Upon reaching a steady target temperature (typically under 10 mins), we modulate the light source's heat flux periodically. This approach significantly decreases the total time for characterization and increases testing throughput. Similar to Hatta et al.'s approach [12], we partially block the light source such that only the center of the sample is heated. However, several key difference exist. First, in Hatta's work samples were heated to high temperatures (up to 500 °C) from the surroundings. Second, in Hatta et al.'s work the radiation losses were linearized, whereas in our case temperature gradients along the direction of heat conduction exist even under steady heating, and nonlinear radiation losses are included in the model. Thirdly, Hatta's work requires thermocouples for temperature detection. In our study, an infrared (IR) camera calibrated up to 2000 °C is employed

for non-contact and non-intrusive temperature detection. Moreover, IR thermography offers data-rich temperature profiles that increase measurement reliability [18] and decrease uncertainties for parameters of interest [19]. Here, we employ a Bayesian framework that benefits from the data-rich IR thermography to quantify uncertainty rigorously for the parameters of interest.

2 Physical system modeling

Existing Ångström's methods for high temperature characterization employ linearized radiation loss models [9] [13] [15] [12]. These methods can be accurate if the sample's temperature T remains uniform along the direction of heat conduction and if the temperature oscillation amplitude is negligible compare to T. In this work, a thin disk sample (88.50 mm OD) is partially heated using a concentrated light source and relatively significant temperature gradient exists along the heat conduction direction. Therefore, radiation losses can not be linearized, and we instead develop a numerical solution to account for non-linear radiation loss.

The schematic of our system is shown in Fig. 1A. The concentrated light source is a 10 kW Xenon short arc lamp with Lorentzian intensity distribution [20] [21]. The power of the concentrated light source is controlled using a 0-10 V external control voltage. The heat flux of the light source is given as:

$$q_s''(r,V) = \frac{A(V)}{\pi} \frac{\sigma_{solar}}{\sigma_{solar}^2 + r^2} \tag{1}$$

where $A(V)$ is nominal peak heat flux and is determined by the control voltage V, and σ_{solar} indicates the width of the distribution and is determined by the reflector of the light source and is relatively independent of V; r is the radius on the sample. We use a function generator to produce sinusoidal voltage signals to control the light source to output periodic heat flux. Details for characterizing and modeling the light source are provided in the Supplemental Materials S1.

In our study the concentrated light source is partially blocked by three annular tungsten rings (referred to as light blockers) so that only the center of the sample is exposed to the light source. A custom tray tracing code [21] was employed to evaluate the intensity distribution of the concentrated light source as truncated by the light blockers. The simulated intensities with and without truncation are shown in Fig. 1B. A window function, defined by the ratio of intensities with and without light blocker are shown in Fig. 1C. As shown by the the window function, the light blockers only affect the intensity distribution near the inner edge of the light blocker. The window function in Fig. 1C shows the simulated truncated intensity distribution with the light blockers.

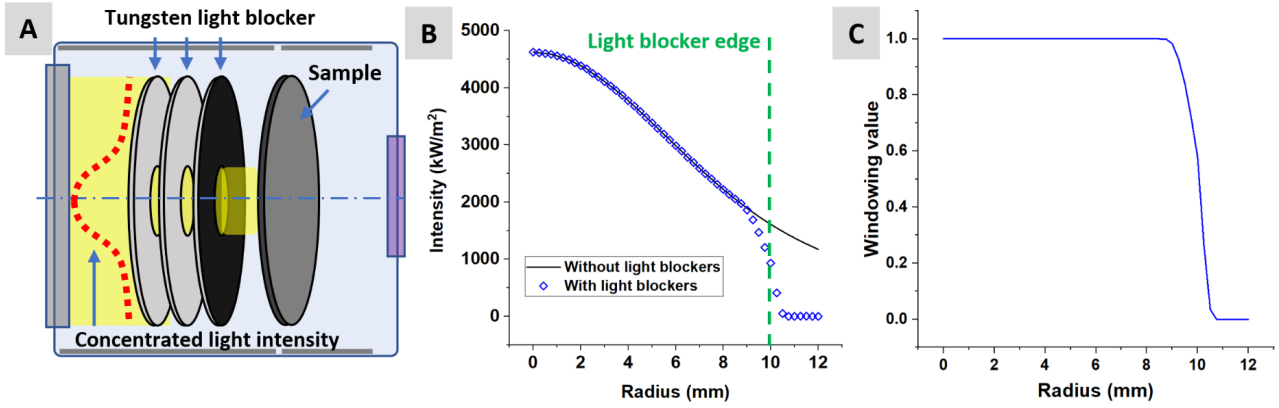

Fig. 1. (A) Schematic of the experimental system for thermal diffusivity characterization. (B) Ray tracing study for intensity distribution of the concentrated light source with and without light blockers. (C) A window function to model the truncated Lorentzian intensity distribution.

Having introduced the concentrated light source, we present a finite difference solver for the transient heating process, under the following assumptions to simplify the analysis:

1. The fin approximation is made for these thin disk samples, because the thermal penetration depth is much larger than the sample thickness [12].
2. All surfaces are gray and diffuse.
3. Thermal expansion of the sample is not considered.
4. Heat loss via conduction and convection are neglected.
5. To facilitate IR thermography, a thin layer of high-emissivity coating was applied to the back side of the sample. This layer contributes approx. 2% to the total sample mass and is not considered in the model.
6. We use the following expression [22–24] for temperature-dependent thermal diffusivity:

$$\alpha(T) = \frac{1}{A_\alpha \times T + B_\alpha} \tag{2}$$

This empirical form has been shown to fit a broad range of conditions, largely because it captures the main effects of increased thermal carrier scattering with increasing temperature.

A schematic of the finite difference network is shown in Fig. 2A along with a control volume (dashed green box) for a node m at time step p. Applying conservation of energy to the control volume shown in Fig. 2A we obtain:

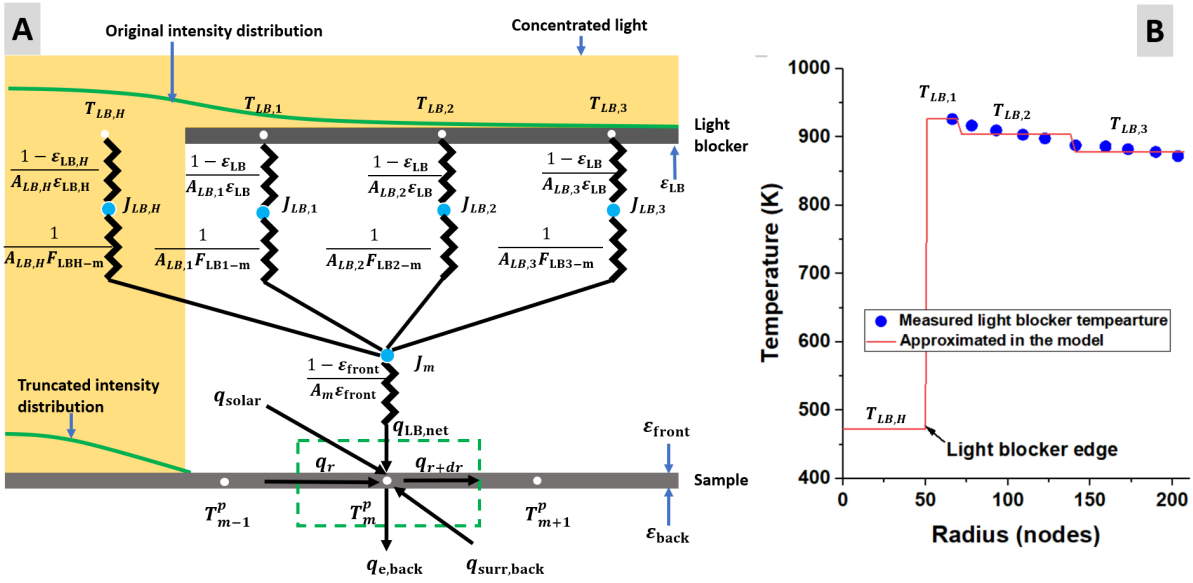

Fig. 2. (A) Finite difference scheme for the transient heating process with the radiation network. The green dashed rectangular box indicates a control volume for node m on the sample at time step p. The yellow area indicates the concentrated light and the green solid lines indicate the intensity distribution before and after the light blockers. (B) Temperature distributions on the light blocker. For simplicity, we use three discrete temperatures for modeling.

$$q_r - q_{r+dr} + q_{solar} + q_{lb,net} - q_{e,back} + q_{surr,back} = \dot{E} \tag{3}$$

where q_r and q_{r+dr} indicate heat transfer via conduction, expressed as:

$$q_r = r d\theta\, dz\, \ddot{q_r}, \text{where } \ddot{q_r} = -k\frac{\partial T}{\partial r} \tag{4}$$

$$q_{r+dr} = q_r + \frac{\partial q_r}{\partial r}dr = q_r - \frac{\partial(r d\theta\, dz\, k\frac{\partial T}{\partial r})}{\partial r}dr \tag{5}$$

q_{solar} indicates energy absorbed from the concentrate light source:

$$q_{solar} = \eta\, \ddot{q_s}\, d\theta\, r\, dr \tag{6}$$

where η indicates sample absorptivity from the concentrated light source, and $\ddot{q_s}$ is given in Eq. 1.

The net heat flow between the light blocker and the sample, $q_{lb,net}$, is calculated using a radiation network as shown in Fig. 2A. Based on experimental observations (see Supplemental Materials S3 for light blocker temperature measurements), the temperature gradient of the light blocker along the radial direction is typically low (approx. 50K). Therefore, we use three discrete constant temperatures to approximate the light blocker temperature distribution in different regions as shown in Fig. 2B. We assign $T_{lb,1}$ as the temperature between radius $R_{lb,H}$ and $R_{lb}/3$, where $R_{lb,H}$ is the radius of the light blocker's hole and R_{lb} is the radius of the light blocker. Similarly we assign $T_{lb,2}$, $T_{lb,3}$ and $T_{lb,H}$ for the region bounded by $R_{lb}/3$ to $2R_{lb}/3$, $2R_{lb}/3$ to R_{lb} and 0 to $R_{lb,H}$, respectively. $q_{lb,net}$ is expressed as:

$$\begin{aligned} q_{lb,net} =& \frac{\sigma T_{lb1}^{p4} - T_m^{p4}}{\frac{1-\varepsilon_s}{\varepsilon_s A_m} + \frac{1}{A_{lb1} F_{lb1-m}} + \frac{1-\varepsilon_{lb}}{\varepsilon_{lb} A_{lb1}}} + \frac{\sigma T_{lb2}^{p4} - T_m^{p4}}{\frac{1-\varepsilon_s}{\varepsilon_s A_m} + \frac{1}{A_{lb2} F_{lb2-m}} + \frac{1-\varepsilon_{lb}}{\varepsilon_{lb} A_{lb2}}} \\ &+ \frac{\sigma T_{lb3}^{p4} - T_m^{p4}}{\frac{1-\varepsilon_s}{\varepsilon_s A_m} + \frac{1}{A_{lb3} F_{lb3-m}} + \frac{1-\varepsilon_{lb}}{\varepsilon_{lb} A_{lb3}}} + \frac{\sigma T_{lbH}^{p4} - T_m^{p4}}{\frac{1-\varepsilon_s}{\varepsilon_s A_m} + \frac{1}{A_{lbH} F_{lbH-m}} + \frac{1-\varepsilon_{lb}}{\varepsilon_{lb} A_{lbH}}} \\ &= q_{m,lb} - C_{m,lb}\, \sigma T_m^{p4} \end{aligned} \tag{7}$$

where σ is the Stefan-Boltzmann constant; ε_{lb} is the emissivity of the light blocker; and ε_{front} is the emissivity of the front side of the sample. A_{lbH}, A_{lb1}, A_{lb2} and A_{lb3} are the light blocker areas corresponding to discrete temperatures T_{lbH}, T_{lb1}, T_{lb2} and T_{lb3} respectively. F_{lbH-m}, F_{lb1-m}, F_{lb2-m}, F_{lb3-m} are view factors from A_{lbH}, A_{lb1}, A_{lb2} and A_{lb3} to the differential ring element at node m. $C_{m,lb}$ and $q_{m,lb}$ are expressed as:

$$\begin{aligned} C_{lb,m} =& \frac{1}{\frac{1-\varepsilon_s}{\varepsilon_s A_m} + \frac{1}{A_{lb1} F_{lb1-m}} + \frac{1-\varepsilon_{lb}}{\varepsilon_{lb} A_{lb1}}} + \frac{1}{\frac{1-\varepsilon_s}{\varepsilon_s A_m} + \frac{1}{A_{lb2} F_{lb2-m}} + \frac{1-\varepsilon_{lb}}{\varepsilon_{lb} A_{lb2}}} \\ &+ \frac{1}{\frac{1-\varepsilon_s}{\varepsilon_s A_m} + \frac{1}{A_{lb3} F_{lb3-m}} + \frac{1-\varepsilon_{lb}}{\varepsilon_{lb} A_{lb3}}} + \frac{1}{\frac{1-\varepsilon_s}{\varepsilon_s A_m} + \frac{1}{A_{lbH} F_{lbH-m}} + \frac{1-\varepsilon_{lb}}{\varepsilon_{lb} A_{lbH}}} \end{aligned} \tag{8}$$

$$q_{lb,m} = \frac{\sigma T_{lb1}^{p4}}{\frac{1-\varepsilon_s}{\varepsilon_s A_m} + \frac{1}{A_{lb1} F_{lb1-m}} + \frac{1-\varepsilon_{lb}}{\varepsilon_{lb} A_{lb1}}} + \frac{\sigma T_{lb2}^{p4}}{\frac{1-\varepsilon_s}{\varepsilon_s A_m} + \frac{1}{A_{lb2} F_{lb2-m}} + \frac{1-\varepsilon_{lb}}{\varepsilon_{lb} A_{lb2}}} + \frac{\sigma T_{lb3}^{p4}}{\frac{1-\varepsilon_s}{\varepsilon_s A_m} + \frac{1}{A_{lb3} F_{lb3-m}} + \frac{1-\varepsilon_{lb}}{\varepsilon_{lb} A_{lb3}}} + \frac{\sigma T_{lb4}^{p4}}{\frac{1-\varepsilon_s}{\varepsilon_s A_m} + \frac{1}{A_{lbH} F_{lbH-m}} + \frac{1-\varepsilon_{lb}}{\varepsilon_{lb} A_{lbH}}} \tag{9}$$

$q_{e,back}$ indicates radiation loss at the back side of the sample:

$$q_{e,back} = \varepsilon_{back} \sigma T^4 d\theta r dr \tag{10}$$

where ε_{back} is the emissivity of the back side of the sample.

The term $q_{surr,back}$ indicates the rate of radiation absorbed by the back side of the sample. We assume the surrounding temperature in the vacuum chamber at the back side of the sample is constant. Therefore, $q_{surr,back}$ is also a constant. More details for calculating $q_{surr,back}$ are provided in the supplemental material S1.

The energy accumulation term $\dot{E}$ is expressed as:

$$\dot{E} = d\theta r dr dz \rho c_p \frac{\partial T}{\partial t} \tag{11}$$

Substitution of Eqs. 4-11 into the governing equation Eq. 3 yields:

$$\frac{\partial}{\partial r}\left(k\frac{\partial T}{\partial r}\right) + \frac{1}{r}\left(k\frac{\partial T}{\partial r}\right) + \frac{\dot{q_s}}{dz} - \frac{(\varepsilon_{back} + C_{lb,m}/(d\theta r dr))\sigma T^4}{dz} + \frac{q_{lb,m} + q_{surr,back}}{r dr d\theta dz} = \rho c_p \frac{\partial T}{\partial t} \tag{12}$$

The initial (IC) and the boundary (BC) conditions are:

$$\begin{cases} \text{IC: } t = 0,\ T(x,0) = T_i & \text{(13a)} \\ \text{BC: } r = R,\ -k\dfrac{\partial T}{\partial r} = \sigma(\varepsilon T^4 - \eta T_W^4) & \text{(13b)} \\ \text{has to satisfy: } \dfrac{\partial T}{\partial r}|_{r=0} = 0 & \text{(13c)} \end{cases}$$

where T_W indicates the temperature of the vacuum chamber wall. Eq. 12 is discretized using a central-difference implicit finite difference scheme. A detailed discussion of the finite difference scheme and the implicit Newton-Raphson solver are given in the supplemental material S2. A mesh independence analysis has been performed to ensure the convergence of the numerical solution (see Supplemental Materials S2). The total number of nodes along the radial direction is 220.

Having obtained the simulated temperature profiles, we next extract amplitude and phase from the simulation results. First, we choose a reference radius R_0 that is close to the inner diameter of the light blocker but not irradiated by the concentrated light source. We also choose a region of analysis bounded by the reference radius R_0 and an outer bound R_N, in which significant amplitude decay is observed. Our code automatically detects quasi steady-state oscillation when the maximum mean temperature rise within one cycle is less than 0.1% compared to the oscillation amplitude, as shown in Fig. 3A. Amplitude decay and phase shift for all nodes are calculated with respect to the temperature profile at the reference radius. Representative amplitude decay and phase shift plots are shown in Fig. 3B and 3C respectively.

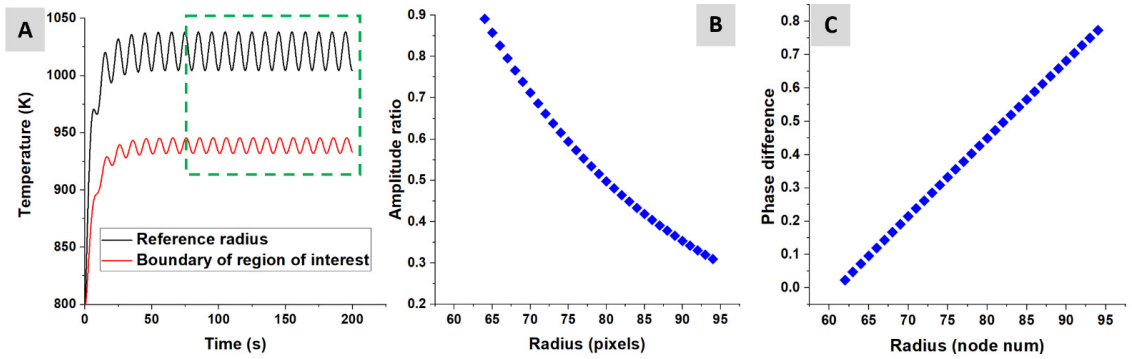

Fig. 3. (A) Simulated temperature profile at the reference radius and the boundary of the region of analysis. (B) Amplitude decay of temperature profiles within the region of analysis. (C) Phase shift of temperature profiles within the region of analysis.

3 Experimental techniques

3.1 Experimental setup

In this work, the samples under test are thin disks (graphite: 0.92 mm, copper: 0.79 mm) with 88.50 mm outer diameter. Measurements were conducted under vacuum, and the vacuum level was approx. 0.05 Torr. The heat source is a 10 kW Xenon short arc lamp (Superior: SQP-SX10000FXT), and an electroformed parabolic reflector (Optiforms, Ag coated) concentrates the light. The inner diameter of the light blockers is 20.0 mm, and the distance between neighboring light blockers is 0.90 mm. A sample holder is designed to hold the light blockers and the sample concentrically as shown in Fig. 4A. The sample is fixed to the sample holder using four pairs of small thermally insulating ceramic washers to minimize heat losses via conduction. The distance between the sample and the neighboring light blocker is 1.60 mm. We use three light blockers so that temperature oscillation on the last light blocker is minimal. The last light blocker facing the sample is coated with a thin layer of high-emissivity coating (Aremco 840CMX) to reduce radiative reflection from the sample and enable temperature measurements using IR themography. We use an IR camera (Flir A655sc, calibrated to 2000 °C) for temperature measurements. A schematic of the system is shown in Fig. 4B, and a photograph of the system is shown in Fig. 4C.

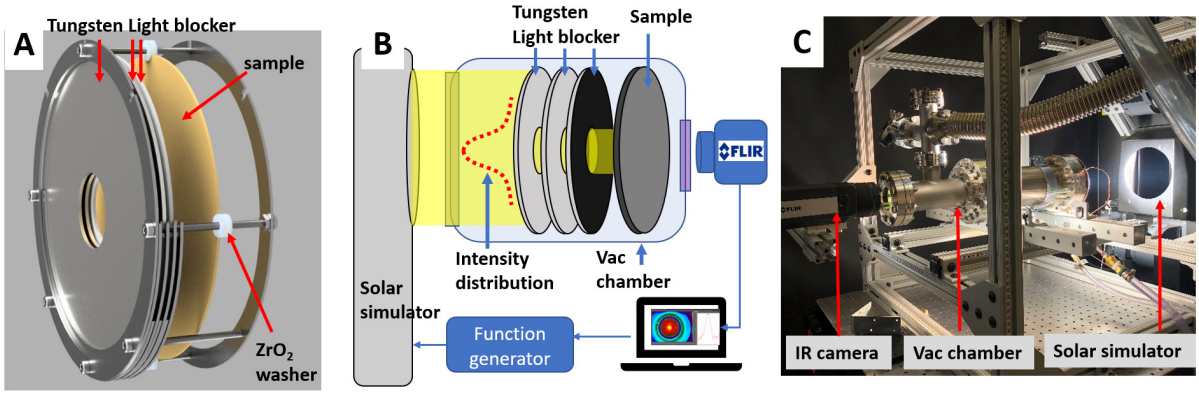

Fig. 4. (A) Tungsten light blockers and the sample holder for measurements. (B) Schematic of the system. (C) a photograph of the system.

The concentrated light source is powered by a 3-phase power supply with fixed 110 V with programmable current ranging from 100 to 200 A. The operating current is controlled externally using a 0-10 V function generator. Within the range of operation, the concentrated light source exhibits a linear relationship between external control voltage and the operating current. To heat the sample to high temperatures, we first control the solar simulator to produce steady heat flux.

Upon reaching steady temperature (typically in 10 min), we modulate the function generator to output biased sinusoidal control voltage signals. Because of the linear relationship between external control voltage and the operating current, the concentrated light source also outputs biased sinusoidal heat flux. When the system reaches quasi steady-state oscillation (approx.1 min after introducing the oscillating heat flux), we start recording the temperature profiles using the IR camera.

3.2 IR thermography and processing

To facilitate IR thermography, the back side of the sample is coated with a thin layer of high-emissivity coating (Aremco, 840MX). Our IR camera uses uncooled microbolometer detector with spectral range between 7.5-14 μm. From the spectral emissivity of the coating between 7.5-14 μm [25], we estimated the total emissivity in the IR camera's range is between 0.88 and 0.92. Because the coating's spectral emissivity is relatively independent of temperature, we measured its emissivity using a thermocouple (type K, $\pm$0.75% accuracy) and the IR camera at relatively lower temperatures (370 °C), and the emissivity was 0.92. Therefore, we use 0.92 as the sample's emissivity for IR measurement. The temperature measurement error for the IR camera is approx. $\pm$2% [26].

Because of symmetry, the isothermal lines in the IR image are concentric circles, as shown in Fig. 5A. At steady state, temperature measured for a pixel located at R_0 exhibits much stronger noise in a high temperature environment as compared to a room temperature condition, as illustrated in Fig. 5B. To reduce high random noise, we developed a computationally efficient method using bi-linear interpolation to obtain the average temperature at a given radius. The averaged temperature profiles at two representative locations R_0 and R_N are shown in Fig. 5C. Details of the IR image processing are available in the supplemental material S4. We employ a parallel approach to average all the IR images in a recorded video, and the time required to fully process an IR recording consists of 500 images is less than one minute.

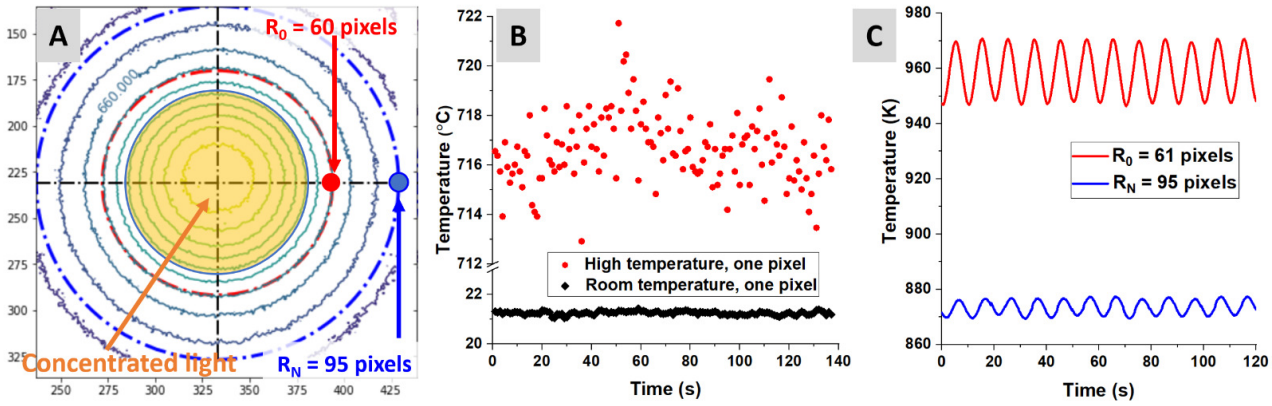

Fig. 5. (A) Temperature contour plot of a sample. The area exposed to the concentrated light source is indicated by the yellow circle. (B) Steady temperature profile at pixel R_0 at room and high temperatures. (C) Averaged temperature profile at two representative radii R_0 and R_N.

Having obtained averaged temperature profiles at different radii, we extract amplitude decay and phase shift with respect to the reference radius R_0. We employ a Fourier transform to calculate amplitude decay and phase shift for two sinusoidal temperature signals [27]. The main benefit of working with amplitude decay and phase shift instead of absolute temperature is the robustness against emissivity [28] [18] [19]. For the high-emissivity coating, a slight variation of the emissivity setting in the IR camera from 0.92 to 0.88 causes approx. 20 K difference in absolute temperature, as shown in Fig. 6A. Because emissivity affects only absolute temperature and does not change the shape of the oscillating temperature profiles, intuitively, the phase of a sinusoidal temperature profile is not affected by the emissivity setting in the IR camera. Therefore, phase difference can be accurately measured even if emissivity is not known precisely, as shown in Fig. 6B.

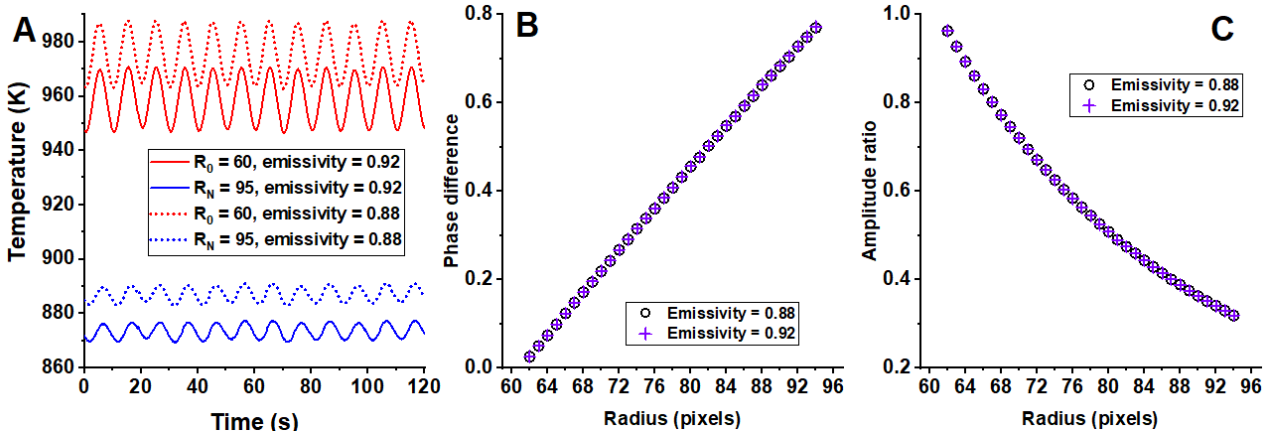

Fig. 6. (A) Temperature profiles measured at R_0 and R_N using different emissivity settings. (B) Phase difference calculated using temperature profiles between R_0 and R_N under different emissivity settings. (C) Amplitude decay calculated using temperature profiles between R_0 and R_N under different emissivity settings.

For amplitude decay, we consider arbitrary locations R_x on the sample. If we neglect the effect of the surroundings, the radiation measured by the IR camera is proportional to the radiation emission at R_x. We denote the true emissivity at R_x as ε and true temperature as T_x, whereas the emissivity setting in the IR camera is $\varepsilon^{'}$ and the corresponding measured temperature is $T_x^{'}$. The following equation assumes that the IR camera measures radiance correctly:

$$\sigma\varepsilon^{'}T_x^{'4} = \sigma\varepsilon T_x^4 \tag{14}$$

Because of oscillating heat flux, the true peak-to-valley temperature change is ΔT, and the temperature change observed in the IR camera is $\Delta T^{'}$. Considering two locations on the sample R_0 and R_x, and based on Eq. 14, we obtain the following relationships:

$$\begin{cases} \sigma\varepsilon^{'}(T_0^{'}+\Delta T_0^{'})^4 = \sigma\varepsilon(T_0+\Delta T_0)^4 & \text{(15a)} \\ \sigma\varepsilon^{'}(T_x^{'}+\Delta T_x^{'})^4 = \sigma\varepsilon(T_x+\Delta T_x)^4 & \text{(15b)} \end{cases}$$

The amplitude decay can be expressed as:

$$\frac{\Delta T_x^{'}}{\Delta T_0^{'}} = \frac{\gamma(T_x+\Delta T_x)-T_x^{'}}{\gamma(T_0+\Delta T_0)-T_0^{'}} \tag{16}$$

where $\gamma = (\varepsilon/\varepsilon^{'})^{1/4}$. Based on Eq. 14, we also have:

$$\sigma\varepsilon^{'}(T_0^{'})^4 = \sigma\varepsilon(T_0)^4,\ T_0^{'} = \gamma T_0 \tag{17}$$

As a result, γ cancels, and the ratio of oscillation amplitude shows no dependence on emissivity. Fig. 6C shows that amplitude

decay extracted from temperature profiles does not depend on emissivity.

$$\frac{\Delta T_x^{'}}{\Delta T_0^{'}} = \frac{\Delta T_x}{\Delta T_0} \tag{18}$$

To summarize, the averaging of the IR image over the radius significantly reduces random noise in the high-temperature environment. The averaging approach is computationally efficient and requires less than 1 min to process an IR recording typically consisting of 500 IR images. We demonstrate that amplitude decay and phase shift extracted from measured temperature profiles are not affected by errors in emissivity, and therefore we work with amplitude decay and phase shift instead of absolute temperature profiles.

4 Model sensitivity analysis

In this study, we employ a full factorial design of experiments at two levels [29] to investigate the sensitivity of the physical model output (amplitude decay and phase shift) to the parameter of interest (thermal diffusivity). Here we use graphite's properties for demonstration. In addition to the parameter of interest, we are uncertain about several others. First, the intensity distribution of the concentrated light source is difficult to characterize precisely. Based on a previous study for a similar concentrated light source [21] and our preliminary investigation using a calorimetry method, the estimated intensity distribution width (σ_{solar}) is 0.01 m. We assume a $\pm 30\%$ variation associated with σ_{solar}. Secondly, in our study the light blocker temperature T_0 is difficult to measure precisely. We assume a $\pm 5\%$ variation associated with T_0 and assume the light blocker temperature is uniform and constant for sensitivity analysis. Lastly, we treat thermal diffusivity as a temperature-independent parameter for sensitivity analysis. For a typical graphite sample the estimated thermal diffusivity α at 1000 K is $2.2 \times 10^{-5}\,\mathrm{m}^2/\mathrm{s}$. We assigned a relatively low range of variation ($\pm 5\%$) for α. Table 1 shows a summary of these parameters and the corresponding range of variations. We employ a main effect approach [29] to quantify model output sensitivity to

Table 1. Parameters for a two level full factorial design of experiment

Parameter	Definition	Range
α	Thermal diffusivity	(2.09,2.31) $\times 10^{-5}\mathrm{m}^2/\mathrm{s}$, 5% variation
σ_{solar}	Light source intensity distribution	(0.7,1.3)$\times 10^{-2}$ m, 30% variation
T_0	Light blocker temperature	(950, 1050) K, 5% variation

an input parameter θ. For a two-level design, the main effect $ME(\theta)$ is expressed as:

$$ME(\theta) = \frac{1}{2}\left(f(\theta+) - f(\theta-)\right) \tag{19}$$

where f indicates the model, and $\theta+$ and $\theta-$ indicate the model at 'high' and 'low' parameter values. We evaluate the main effect of parameters defined in Table 1 to understand how model outputs (amplitude decay and phase shift) are influenced by input parameter changes. We choose an area ($R_0 = 60$ pixels with 12 pixels span) that is not irradiated by the concentrated light for amplitude and phase calculations. This area is chosen because of high signal-to-noise ratio based on experimental observation. A prior study showed that increased heating frequency is beneficial to enhance sensitivity in thermal diffusivity [19].

In this study, the concentrated light source is modulated sinusoidally to apply periodic heating to samples. We limit the periodic heating frequency to 0.15 Hz due to safety and operational stability of the Xenon light bulb [30]. The lower

limit of the heating frequency is 0.02 Hz because of the lengthy measurement time at low heating frequencies. The main effect results for amplitude decay of selected input parameters are shown in Fig. 7 (top row). Similar to a prior study [19], sensitivity in thermal diffusivity increases with the heating frequency. For relatively fast heating frequencies ($f_{heating} \geq 0.08$ Hz), emissivity and light blocker temperature exhibit low sensitivity. We also observe that the intensity distribution width σ_{solar} contributes little to the main effect. This finding is advantageous compared to Hatta et al.'s approach [12], Cowan's approach [15] and the laser flash method [1], each of which are sensitive to the intensity distribution of the light source. The main effect results calculated using phase shift are shown in Fig. 7 (bottom row). Similarly, faster heating frequencies are advantageous for thermal diffusivity detection, and σ_{solar} makes an insignificant contribution to the main effect.

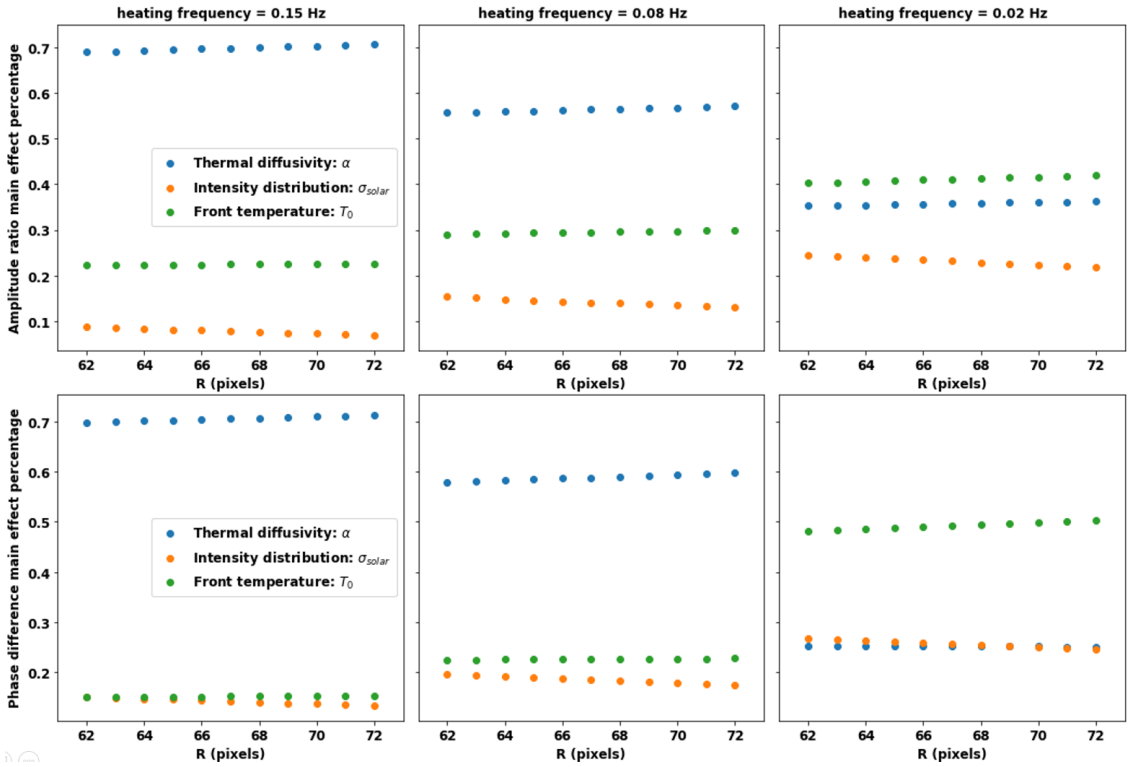

Fig. 7. Top row: percentage main effect for amplitude ratio of different parameters at several heating frequencies. Bottom row: percentage main effect for phase difference of different parameters at several heating frequencies.

The foregoing results indicate that high sensitivity for thermal diffusivity can be achieved with $f_{heating} \geq 0.08$ Hz for a graphite sample. The results also indicate that amplitude and phase are insensitive to the intensity distribution of the light source σ_{solar}.

5 Uncertainty quantification and results

5.1 Uncertainty quantification using a Bayesian framework

In this study we estimate thermal diffusivity using amplitude decay and phase shift measurements. Conventional parameter estimation methods convert an inverse problem to an optimization problem by minimizing residuals between measurement results and the physical model. In this case the inverse problem is ill-posed, and the solution is not unique. Also such methods lack rigorous uncertainty estimates for parameters. This study employs a Bayesian framework that incorporates prior knowledge of parameters and measurement processes to produce a complete statistical description of the parameters. Growing interest exists in applying the Bayesian framework to inverse heat transfer problems, and several studies have demonstrated its benefits [19] [31] [32] [33].

The Bayesian framework is based on the Bayes' theorem. Consider a set of parameters θ and measurement results D; the posterior distribution for θ after observing D is expressed using Bayes' theorem:

$$p(\theta|D) = \frac{p(D|\theta)p(\theta)}{p(D)} \tag{20}$$

In this work, D consists of amplitude, phase measurements within a region of analysis and average temperature profiles at inner (R_0) and outer bounds (R_N) of the region. θ consists of four parameters: A_α, B_α, σ_{solar} and T_{bias}. A_α and B_α are the coefficients for temperature-dependent thermal diffusivity and are defined in Eq. 2. In our study, the intensity distribution of the concentrated light source is difficult to characterize precisely. Therefore, we treat σ_{solar} as a unknown parameter and update our state of knowledge for σ_{solar} using the Bayesian framework. Lastly, the light blocker temperature measured using the IR camera (see Supplemental Materials S3 for details) also suffers slight system error because the measurement process differs from real experiments. Therefore, we introduce another parameter T_{bias} to augment the measured light blocker temperature to model the light blocker temperature under real measurement conditions.

The posterior distribution is proportional to the likelihood function $p(D|\theta)$ and the prior distribution $p(\theta)$. The likelihood function $p(D|\theta)$ models the measurement process and indicates the probability of observing data D given parameter θ and measurement noise σ_D. First we consider amplitude decay measurements. We denote measured amplitude decay at radius R_i as ΔA_i and assume that it follows a Gaussian distribution with mean $A[f(\theta)]$ and standard deviation $\sigma_{\Delta A,i}$. $A[f(\theta)]$ indicates the amplitude decay from the physical model f evaluated using parameter θ. For amplitude decay at R_i, the likelihood function is given by.

$$p(\Delta A_i|\theta) \sim \mathcal{N}(\mu = \Delta A_i - A[f(\theta)]_i, \Sigma = \sigma_{\Delta A,i}) \tag{21}$$

Assuming amplitude measurements at different radii are independent, then for all amplitude decay measurements ΔA within the region of analysis, the likelihood function is:

$$p(\Delta A|\theta) \sim \prod_{i=1}^{N} \mathcal{N}(\mu = \Delta A_i - A[f(\theta)]_i, \Sigma = \sigma_{\Delta A,i}) \tag{22}$$

The likelihood functions for all phase shift measurements $\Delta\phi$ within the region of analysis are derived similarly. $\phi[f(\theta)]$ indicates the phase shift from the physical model f evaluated using parameter θ:

$$p(\Delta\phi|\theta) \sim \prod_{i=1}^{N} \mathcal{N}\left(\mu = \Delta\phi_i - \phi[f(\theta)]_i, \Sigma = \sigma_{\Delta\phi,i}\right) \tag{23}$$

In addition, the likelihood functions for the mean temperature profiles at the inner ($T_{mean,R0}$) and outer ($T_{mean,RN}$) bounds of the region of analysis are treated as follows. $T_m([f(\theta)])$ indicates the mean temperature obtained from the physical model f evaluated using parameter θ. σ_T indicates the standard deviation in mean temperature measurements. Unlike amplitude and phase measurements, we manually choose σ_T = 2 K to ensure the mean simulated temperatures within the region of analysis match experimental measurements. Because we use temperature-dependent properties in this study, matching simulated and experimentally measured mean temperatures is important. The likelihood function becomes:

$$p(T_{mean}|\theta) \sim \mathcal{N}(\mu = T_{mean,R0} - T_m([f(\theta)])_0, \Sigma = \sigma_T)\, \mathcal{N}(\mu = T_{mean,RN} - T_m([f(\theta)])_N, \Sigma = \sigma_T) \tag{24}$$

By further assuming that ΔA, $\Delta\phi$, $T_{mean,R0}$ and $T_{mean,RN}$ are statistically independent, the simplified likelihood function becomes:

$$p(D|\theta) = p(\Delta A, \Delta\phi, T_{mean,R0}, T_{mean,RN}|\theta) = p(\Delta A|\theta)p(\Delta\phi|\theta)p(T_{mean,R0}|\theta)p(T_{mean,RN}|\theta) \tag{25}$$

The prior distribution $p(\theta)$ represents the prior knowledge for θ. We assume A_α, B_α, σ_{solar} and T_{bias} are statistically independent. Therefore, $p(\theta)$ is expressed as:

$$p(\theta) = p(A_\alpha)p(B_\alpha)p(\sigma_{solar})p(T_{bias}) \tag{26}$$

Substituting the likelihood function (Eq. 25) and the prior distribution (Eq. 26) into the Bayes posterior defined in Eq. 20, the posterior distribution is expressed as:

$$\begin{aligned} p(\theta|D) &= p(A_\alpha, B_\alpha, \sigma_{solar}, T_{bias}|\Delta A, \Delta\phi, T_{mean,R0}, T_{mean,RN}) \\ &= \frac{p(\Delta A, \Delta\phi, T_{mean,R0}, T_{mean,RN}|A_\alpha, B_\alpha, \sigma_{solar}, T_{bias})p(A_\alpha, B_\alpha, \sigma_{solar}, T_{bias})}{p(\Delta A, \Delta\phi, T_{mean,R0}, T_{mean,RN})} \\ &\sim \prod_{i=1}^{N} \mathcal{N}(\mu = \Delta A_i - A[f(\theta)]_i, \Sigma = \sigma_{\Delta A,i})\, \mathcal{N}\left(\mu = \Delta\phi_i - \phi[f(\theta)]_i, \Sigma = \sigma_{\Delta\phi,i}\right) \\ &* \mathcal{N}(\mu = T_{mean,R0} - T_m([f(\theta)])_0, \Sigma = \sigma_T)\, \mathcal{N}(\mu = T_{mean,R0} - T_m([f(\theta)])_N, \Sigma = \sigma_T)\, p(A_\alpha)p(B_\alpha)p(\sigma_{solar})p(T_{bias}) \end{aligned} \tag{27}$$

For an arbitrary distribution with unknown normalization constant, the Markov chain Monte Carlo (MCMC) method is typically used to obtain random samples to reconstruct such a distribution. The most commonly used MCMC algorithm is random walk Metropolis [34] because of its simplicity [31] [32] [19]. However, this algorithm suffers poor convergence and low efficiency for problems with large parameter spaces [35]. To expand the exploration of the parameter space and to improve convergence of the Markov chain, our work employs a No-U-Turn(NUT) sampler [36]. In addition, MCMC requires frequent evaluations of the physical model to calculate the likelihood function. This becomes infeasible for numerical models that require lengthy execution times. A previous study [32] demonstrated significant time efficiency improvement using polynomial chaos for an inverse heat transfer problem. In this study, we develop a non-intrusive polynomial chaos (order 4) surrogate model using a python module "chaospy" [37] to accelerate the original finite difference model. The surrogate model exhibits high accuracy (maximum 0.5% error) for steady temperature profiles, amplitude decay, and phase shift predictions, yet the execution time is reduced to a few milliseconds from several minutes. We employ the python module pymc3 [38] with custom modifications [39] to implement the NUT sampler.

5.2 NUT sampler's results using a graphite sample

To demonstrate the Bayesian framework and NUT sampler, we first tested an isotropic graphite sample (manufacturer:Entegris, grade:TM). The sample's thickness is 0.92 mm with outer diameter 88.50 mm. The density of the graphite sample is 1740 kg/m^3. We used a polynomial fit for specific heat [40] as:

$$c_p(T) = 2245 + 4.56 \times 10^{-2}T - 5.61 \times 10^5/T + 2.77 \times 10^7/T^2 \tag{28}$$

The gray emissivity of the graphite is 0.77, and we coated a layer of thin layer of diffuse high-emissivity (0.88) material on the back side of the sample to facilitate IR thermography. We modulated the light source using a 0.1 Hz voltage signal to achieve relatively high sensitivity in thermal diffusivity. We heated the sample from room temperature to high temperature with 119 A solar simulator current. Steady temperatures were obtained after 10 min, and then a 0.1 Hz oscillation current signal with amplitude 22 A was superimposed on the 110 A bias current. We started the IR recording after approx. one to two minutes when the sample exhibited quasi-steady-state oscillations.

Here we analyze a region on the IR image bounded by $R_0 = 61$ and $R_N = 73$ pixels to obtain temperature profiles and corresponding amplitude decay and phase shift. This region is chosen for high signal-to-noise ratio in both amplitude ratio and phase shift. In addition, the region is chosen to be relatively narrow to keep the temperature difference low (approx. 40 K), such that Eq. 2 remains valid to model thermal diffusivity as a function of temperature.

The results obtained using the NUT sampler are shown in Fig. 8. The top row of subfigures contains the trace plots for four unknown parameters. A trace plot shows the sequential value of a parameter obtained from the NUT sampler. The trace plots exhibit good mixing, and different chains for each parameter oscillate around nearly the same constant value, indicating convergence of the sampling process. The middle row contains histograms obtained from the trace plots of corresponding parameters. The normalized histograms represent the posterior distribution of parameters and indicate the updated state of knowledge given the prior knowledge and the measurement process. The bottom row contains the auto-correlation of the corresponding trace plots in the top row. The auto-correlation decreases rapidly to zero for all parameters, indicating high sampling efficiency.

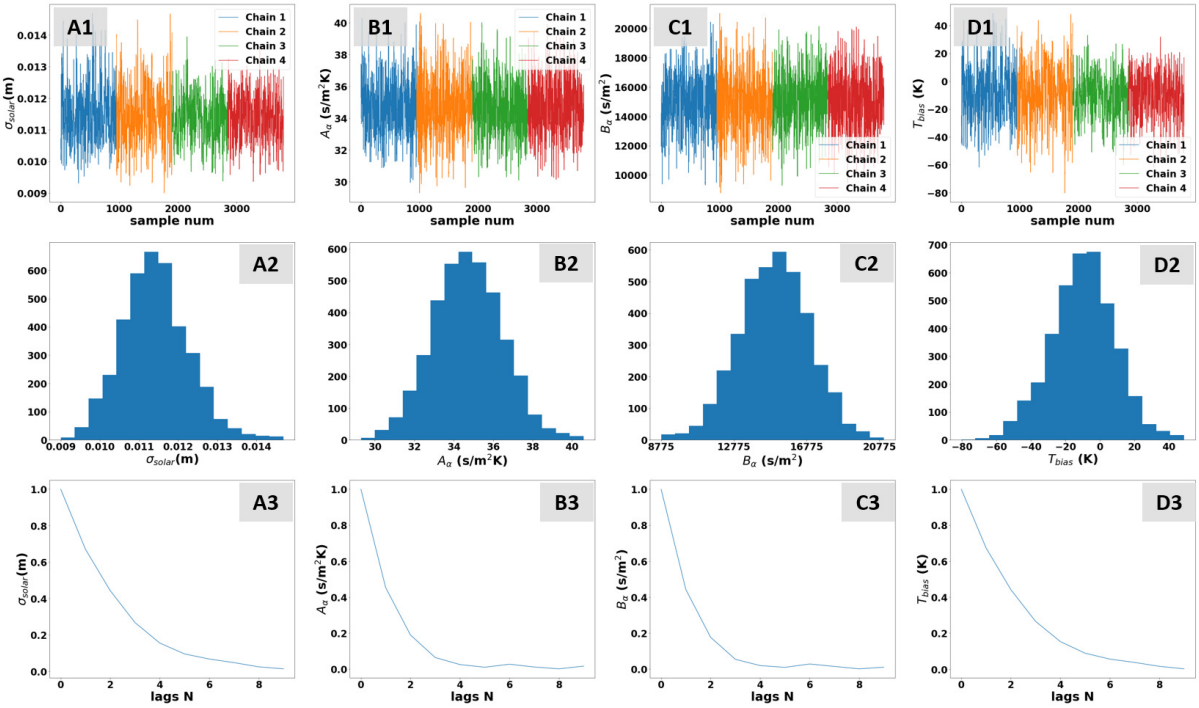

Fig. 8. Top row: Trace plots of parameters. (A1) Intensity distribution width for the concentrated light source σ_{solar}. (B1) and (C1) Parameters for temperature-dependent thermal diffusivity A_α and B_α. (D1) Bias temperature of the light blocker T_{bias}. Middle row: Histograms of the trace plots in the top row. Bottom row: auto-correlation of the trace plots in the top row.

Given the posterior distributions of A_α and B_α, the temperature-dependent thermal diffusivity within the region of analysis (ROA) is shown in Fig. 9. The mean temperatures of the inner and the outer boundary of the ROA are approx. 960 K and 1000 K respectively. The solid line indicate the posterior mean for thermal diffusivity, and the blue band indicates corresponding uncertainty. The same grade graphite samples have been measured using the laser flash method by the man-

ufacturer [40] and are shown as green lines. Good agreement between the posterior results and reference values [40] is observed for the entire temperature range within the ROA.

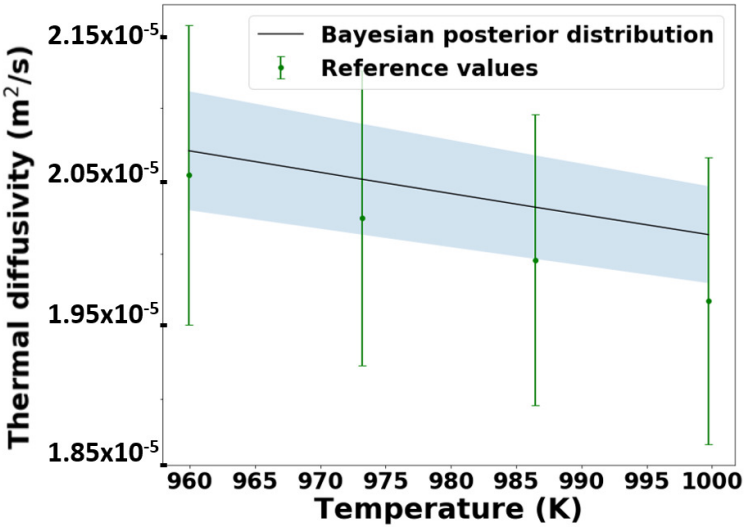

Fig. 9. Thermal diffusivity as a function of temperature evaluated using the posterior mean of A_α and B_α (solid black line) and corresponding uncertainties (blue shade).The reference values are shown as the solid green line [40].

The fitted amplitude (Fig. 10A), phase (Fig. 10B) and temperatures (Fig. 10C) are plotted using the parameters' posterior means, and they match well with experimental measurements.

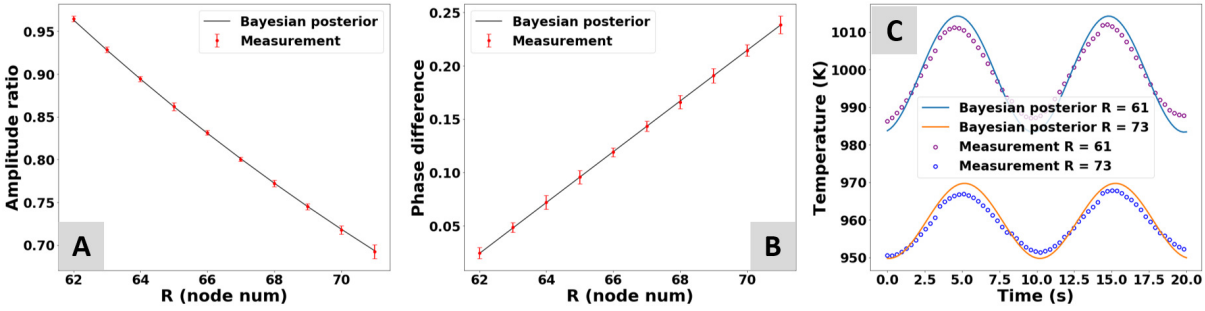

Fig. 10. Fitted (solid black lines) amplitude decay (A), phase shift (B) and temperature profiles at inner and outer boundary of the ROA (C) using the posterior means of parameters from Fig. 8A2-D2.

5.3 Results for graphite at different frequencies and bias voltages

We fixed the bias current of the solar simulator at 119 A and measured multiple graphite samples at different frequencies. Here the tested frequency range is from 0.08 Hz to 0.14 Hz to achieve relatively high sensitivity in thermal diffusivity. We analyze amplitude decay and phase shift within $R_0 = 61$ and $R_N = 73$ pixels, and the results are shown in Fig. 11 in which thermal diffusivity values exhibit good consistency among the different frequencies and multiple samples.

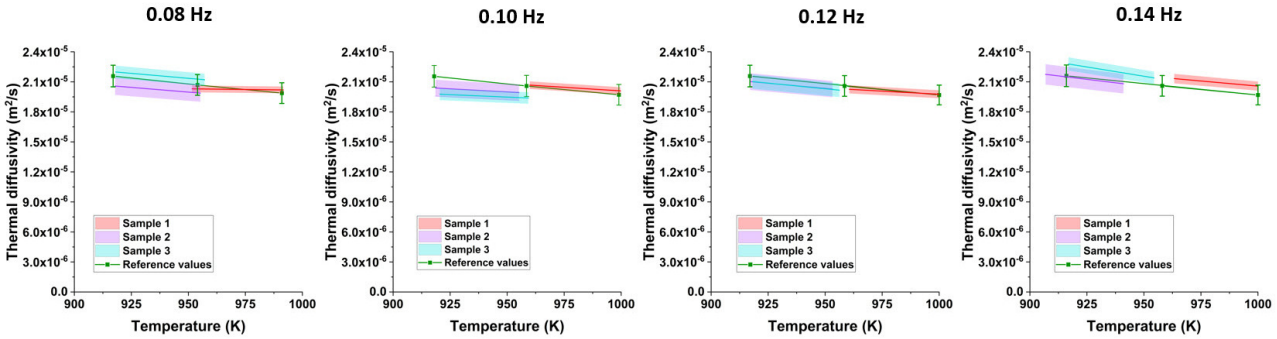

Fig. 11. Thermal diffusivity measured at different frequencies for multiple graphite samples compared to reference values [40]. Note sample 1 exhibits a different temperature range because it was tested with a different light bulb and slightly different reflector condition.

Next, we fixed heating frequency at 0.1 Hz and changed the bias current. Here we choose 119, 152 and 179 A as bias current for the solar simulator and 22 A as the oscillation amplitude. We also explore different region of analysis on the sample. In addition to the region bounded by $R_0 = 61$ and $R_N = 73$ pixels used in previous sections, we analyze another region bounded by $R_0 = 73$ and $R_N = 85$ pixels shown as region 2 in Fig. 12A. This region exhibits lower signal-to-noise ratio compared to region 1, but it also experiences lower temperatures and can extend the temperature measurement range for each test. The results for different currents and different regions are shown in Fig. 12B. We achieve thermal diffusivity measurements over a broader temperature range (220 K) using a wider range of bias currents. The results obtained under different bias currents exhibit good agreement with the reference values [40] over 900 - 1120 K.

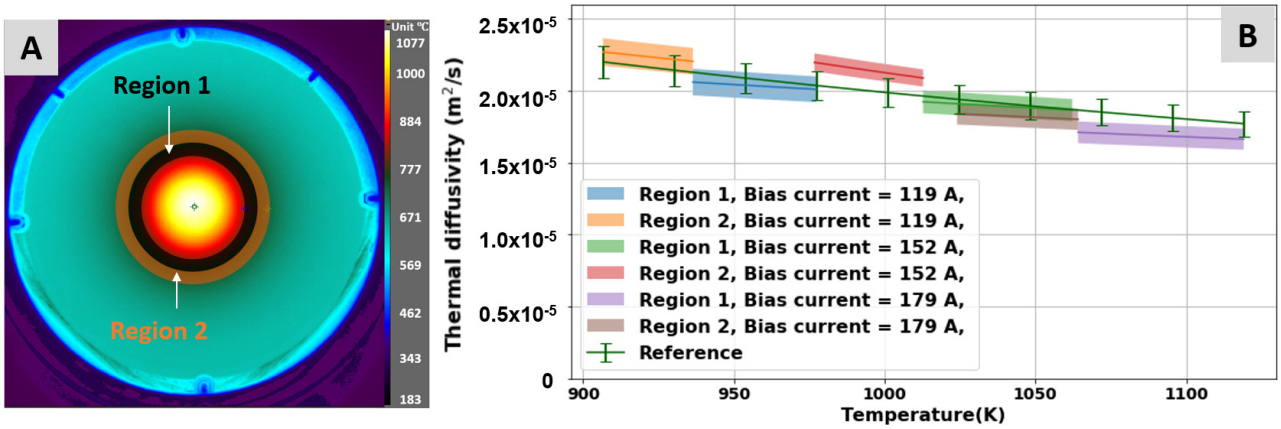

Fig. 12. (A) Region of analysis in an IR image. Region 1 (shaded black) bounded by $R_0 = 61$ and $R_N = 73$ pixels. Region 2 (shaded brown) bounded by $R_0 = 73$ and $R_N = 85$ pixels. (B) Thermal diffusivity measured under different bias currents and in different regions, compared to reference values [40].

5.4 Results for a copper sample

We also tested a copper sample (certified copper 110, 99.9% purity). The sample's thickness is 0.79 mm with outer diameter 88.50 mm. We use a polynomial fit for temperature-dependent specific heat [41]. The copper sample's front and back surfaces were coated with a thin layer of diffuse high-emissivity (0.88) coating (Aremeco, 840MX). The weight contribution of the coating is less than 2% of the sample's total weight and is neglected. The copper sample was measured using 119 A bias current under several different frequencies. The results are shown in Fig. 13, and good agreement with reference values [42] is observed.

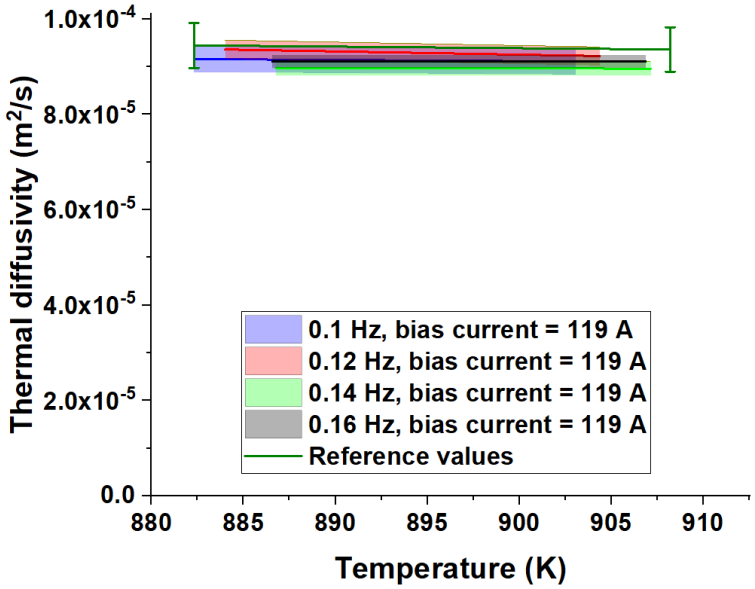

Fig. 13. Thermal diffusivity of copper measured at different heating frequencies with 119 A bias current.

5.5 Limitations of the custom instrument

This work reports a custom Ångström's method for rapid and accurate high-temperature thermal diffusivity characterization. In this section several limitations are presented and should be addressed in future work.

First, the custom instrument and methods reported here are suitable for materials with high diffusivity (*e.g.*, above approx. 1×10^{-5} m^2/s) and thermal properties that are isotropic in the in-plane directions. The concentrated light intensity causes significant temperature gradients and thermal stresses on materials with low diffusivity. As a result, such materials tend to bend or crack during testing. An image for a titanium sample after testing and corresponding measurement results are shown in the Supplemental Material section S6.

Second, compared to past Ångström's methods, the custom instrument requires the quantification of energy input to the sample and energy lost to the surroundings because a temperature gradient exists along the heat conduction direction, and temperature-dependent properties must be used in the model. In addition, an analytical solution does not exist, and the modeling process requires numerical computation, which can be time consuming. However, we developed an accurate and rapid surrogate model to mitigate this issue under the fin approximation, and future work could develop two-dimensional models for thicker samples.

Third, samples under test typically require a high-emissivity coating layer to obtain reliable amplitude decay and phase shift results. Such coatings can deteriorate when temperature increases beyond 1400 °C [25], thus limiting the temperature range for some materials. Damaged coatings can become difficult to remove and make repeated measurement on a single sample difficult.

Fourth, because the focal spot of the concentrated light source is similar in size to the sample's radius, we employed several light blockers so that only the center of the sample is exposed. This approach increases the complexity of the model and experimental setup. A potential improvement is to use an energy source with smaller focal spot, such as a powerful laser source to obviate the need for light blockers.

Fifth, the concentrated light source in this study is not designed to sustains prolonged power fluctuations [30]. We observed relatively fast degradation of bulb life span under oscillating conditions (approx. 100 hrs.) compared to its nominal life span (approx. 800 hrs.). Such performance degradation may lead to variations in testing results.

6 Conclusions

In this work, we present a custom instrument for characterizing thermal diffusivity at high temperatures using a modified Ångström's method. The sample under test is heated directly using a concentrated light source and reaches steady high temperatures rapidly (approx. 10 mins). This is advantageous compared to existing methods that heat samples from surroundings and typically require hours to reach steady high temperatures. We employ non-contact, non-destructive and data-rich IR thermography to measure quasi steady-state oscillating temperature profiles, and an efficient averaging method to process the noisy IR images and obtain temperature profiles with low noise. Amplitude and phase results extracted from such temperature profiles are robust against errors in emissivity. For uncertainty quantification, a surrogate-accelerated Bayesian framework and a NUT sampler are developed to obtain statistical distributions for parameters of interest. For several graphite and copper samples under test, we observe good agreement with reference values under different heating frequencies. We also measure different temperature ranges by adjusting solar simulator current. In general, the results obtained using the custom instrument exhibit approx. 5% difference compared to reference values obtained using the laser flash method. The custom instrument's time efficiency, accuracy, inherent ability to quantify uncertainty rigorously, and relatively low overall cost are expected to benefit researchers for characterizing thermal diffusivity at high temperatures.

Acknowledgements

The authors are grateful for Professor Ilias Bilionis at Purdue University for his free online uncertainty quantification course. The authors thank Professor Jeff Eldredge at UCLA for improving the computational efficiency of the numerical model. The author thank Dr. Michael Barako from Northrop Grumman and Dr. James Wilson from Raytheon Technologies for fruitful feedback on the project. The authors appreciate the help from Ben Alpert of Aremco Products Inc. for high-temperature coating. The authors are grateful for the support from MAE staff Ben Tam, Miguel Lozano, Amanda Gordillo and Marla Cooper during the challenging covid period. This work was supported by the Center for Integrated Thermal Management of Aerospace Vehicles and a UCLA Dissertation Year Fellowship.

References

[1] Parker, W., Jenkins, R., Butler, C., and Abbott, G., 1961. "Flash Method of Determining Thermal Diffusivity, Heat Capacity, and Thermal Conductivity". *J. Appl. Phys.,* **32**(9), pp. 1679–1684.

[2] Clark Iii, L., and Taylor, R., 1975. "Radiation Loss in the Flash Method for Thermal Diffusivity". *J. Appl. Phys.,* **46**(2), pp. 714–719.

[3] Chu, F., Taylor, R., and Donaldson, A., 1980. "Thermal Diffusivity Measurements at High Temperatures by the Radial Flash Method". *J. Appl. Phys.,* **51**(1), pp. 336–341.

[4] Cezairliyan, A., 1984. "A Dynamic Technique for Measurements of Thermophysical Properties at High Temperatures". *Int. J. Thermophys.,* **5**(2), pp. 177–193.

[5] Baba, T., and Cezairliyan, A., 1994. "Thermal Diffusivity of POCO AXM-5Q1 Graphite in the Range 1500 to 2500 K Measured by a Laser-Pulse Technique". *Int. J. Thermophys.,* **15**(2), pp. 343–364.

[6] Gustafsson, S., 1991. "Transient Plane Source Techniques for Thermal Conductivity and Thermal Diffusivity Measurements of Solid Materials". *Rev. Sci. Instrum.,* **62**(3), pp. 797–804.

[7] Healy, J., De Groot, J., and Kestin, J., 1976. "The Theory of the Transient Hot-Wire Method for Measuring Thermal Conductivity". *Physica B+C,* **82**(2), pp. 392–408.

[8] Angström, A., 1863. "XVII. New Method of Determining the Thermal Conductibility of Bodies". *Philos. Mag.,* **25**(166), pp. 130–142.

[9] Sidles, P., and Danielson, G., 1954. "Thermal Diffusivity of Metals at High Temperatures". *J. Appl. Phys.,* **25**(1), pp. 58–66.

[10] Katsura, T., 1993. "Thermal Diffusivity of Silica Glass at Pressures up to 9 GPa". *Phys Chem Miner.,* **20**(3), pp. 201–208.

[11] Xu, Y., Shankland, T., Linhardt, A., Rubie, D., Langenhorst, F., and Klasinski, K., 2004. "Thermal Diffusivity and Conductivity of Olivine, Wadsleyite and Ringwoodite to 20 GPa and 1373 K". *Phys. Earth Planet. Inter.,* **143**, pp. 321–336.

[12] Hatta, I., Sasuga, Y., Kato, R., and Maesono, A., 1985. "Thermal Diffusivity Measurement of Thin Films by Means of an AC Calorimetric Method". *Rev. Sci. Instrum.,* **56**(8), pp. 1643–1647.

[13] Abeles, B., Cody, G., and Beers, D., 1960. "Apparatus for the Measurement of the Thermal Diffusivity of Solids at High Temperatures". *J. Appl. Phys.,* **31**(9), pp. 1585–1592.

[14] Vandersande, J., and Pohl, R., 1980. "Simple Apparatus for the Measurement of Thermal Diffusivity between 80–500 K using the Modified Ångström method". *Rev. Sci. Instrum.,* **51**(12), pp. 1694–1699.
[15] Cowan, R., 1961. "Proposed Method of Measuring Thermal Diffusivity at High Temperatures". *J. Appl. Phys.,* **32**(7), pp. 1363–1370.
[16] Wheeler, M., 1965. "Thermal Diffusivity at Incandescent Temperatures by a Modulated Electron Beam Technique". *Br. J. Appl. Phys.,* **16**(3), p. 365.
[17] Tanaka, T., and Suzuki, H., 1972. "The Thermal Diffusivity of Pyrolytic Graphite at High Temperatures". *Carbon,* **10**(3), pp. 253–257.
[18] Hahn, J., Reid, T., and Marconnet, A., 2019. "Infrared Microscopy Enhanced Angstrom's Method for Thermal Diffusivity of Polymer Monofilaments and Films". *J of HEAT TRANSFER-TRANSACTIONS OF THE ASME,* **141**(8), p. 081601.
[19] Hu, Y., and Fisher, T., 2020. "Accurate Thermal Diffusivity Measurements Using a Modified Ångström's Method With Bayesian Statistics". *J of HEAT TRANSFER-TRANSACTIONS OF THE ASME,* **142**(7), p. 071401.
[20] Gomez-Garcia, F., Santiago, S., Luque, S., Romero, M., and Gonzalez-Aguilar, J., 2016. "A New Laboratory-Scale Experimental Facility for Detailed Aerothermal Characterizations of Volumetric Absorbers". In AIP Conference Proceedings, Vol. 1734, AIP Publishing LLC, p. 030018.
[21] Abuseada, M., Ophoff, C., and Ozalp, N., 2019. "Characterization of a New 10 kWe High Flux Solar Simulator via Indirect Radiation Mapping Technique". *J. Sol. Energy Eng.,* **141**(2).
[22] Seipold, U., 1998. "Temperature Dependence of Thermal Transport Properties of Crystalline Rocks—a General Law". *Tectonophysics,* **291**(1-4), pp. 161–171.
[23] Miao, S., Li, H., and Chen, G., 2014. "Temperature Dependence of Thermal Diffusivity, Specific Heat Capacity, and Thermal Conductivity for Several Types of Rocks". *J. Therm. Anal. Calorim.,* **115**(2), pp. 1057–1063.
[24] Abdulagatova, Z., Kallaev, S., Omarov, Z., Bakmaev, A., Grigor'ev, B., and Abdulagatov, I., 2020. "Temperature Effect on Thermal-Diffusivity and Heat-Capacity and Derived Values of Thermal-Conductivity of Reservoir Rock Materials". *GEOMECH GEOPHYS GEO.,* **6**(1), pp. 1–23.
[25] Aremco Products Inc., "High Temperature High Emissivity Coatings," Aremco Product Inc., Accessed Feb 02, 2020, https://www.aremco.com/high-emissivity-coatings/.
[26] FLIR Systems, Inc., 2017. "User's Manual FLIR A6xx Series". FLIR Systems, Inc., Accessed Feb 02, 2020, https://www.flir.com/products/a655sc/.
[27] Hu, Y., Brahim, S., Maat, S., Davies, P., Kundu, A., and Fisher, T., 2020. "Rapid Analytical Instrumentation for Electrochemical Impedance Spectroscopy Measurements". *J. Electrochem. Soc.,* **167**(2), p. 027545.
[28] Visser, E., Versteegen, E., and van Enckevort, W., 1992. "Measurement of Thermal Diffusion in Thin Films using a Modulated Laser Technique: Application to Chemical-Vapor-Deposited Diamond Films". *J. Appl. Phys.,,* **71**(7), pp. 3238–3248.
[29] Montgomery, D., 2017. *Design and Analysis of Experiments*. John Wiley & Sons.
[30] Superior Quartz Products, INC., "Lamp Characteristics and Description," Superior Quartz Products, INC., Accessed Feb 02, 2020, https://www.sqpuv.com/PDFs/TechnicalSpecificationGuide.pdf.
[31] Wang, J., and Zabaras, N., 2004. "A Bayesian Inference Approach to the Inverse Heat Conduction Problem". *Int. J. Heat Mass Transf.,* **47**(17-18), pp. 3927–3941.
[32] Rynn, J., Cotter, S., Powell, C., and Wright, L., 2019. "Surrogate Accelerated Bayesian Inversion for the Determination of the Thermal Diffusivity of a Material". *Metrologia,* **56**(1), p. 015018.
[33] Xu, X., Zhang, Q., Hao, M., Hu, Y., Lin, Z., Peng, L., Wang, T., Ren, X., Wang, C., Zhao, Z., et al., 2019. "Double-Negative-Index Ceramic Aerogels for Thermal Superinsulation". *Science,* **363**(6428), pp. 723–727.
[34] Metropolis, N., Rosenbluth, A., Rosenbluth, M., Teller, A., and Teller, E., 1953. "Equation of State Calculations by Fast Computing Machines". *J. Chem. Phys.,* **21**(6), pp. 1087–1092.
[35] Brooks, S., Gelman, A., Jones, G., and Meng, X., 2011. *Handbook of Markov Chain Monte Carlo*. CRC Press.
[36] Hoffman, M., and Gelman, A., 2014. "The No-U-Turn sampler: Adaptively Setting Path Lengths in Hamiltonian Monte Carlo". *J. Mach. Learn. Res.,* **15**(1), pp. 1593–1623.
[37] Feinberg, J., and Langtangen, P., 2015. "Chaospy: An Open Source Tool for Designing Methods of Uncertainty Quantification". *J. Comput. Sci.,* **11**, pp. 46–57.
[38] Salvatier, J., Wiecki, T., and Fonnesbeck, C., 2016. "Probabilistic Programming in Python using PyMC3". *PeerJ Comput. Sci.,* **2**, p. e55.
[39] Matt Pitkin, 2018, "Using a Black Box Likelihood Function", Matt Pitkin, Accessed Feb 02, 2020, http://mattpitkin.github.io/samplers-demo/pages/pymc3-blackbox-likelihood/.
[40] Entegris, "Graphite Properties and Characteristics," Entegris, Accessed June 19, 2020, https://poco.entegris.com/content/dam/poco/resources/reference-materials/brochures/brochure-graphite-properties-and-characteristics-11043.pdf.
[41] White, G., and Collocott, S., 1984. "Heat Capacity of Reference Materials: Cu and W". *J. Phys. Chem. Ref. Data,*

13(4), pp. 1251–1257.

[42] Touloukian, Y. S., Powell, R. W., Ho, C. Y., and Nicolaou, M. C., 1974. *Thermophysical properties of matter, the TPRC data series. Volume 10. Thermal diffusivity. Data book. 1974*, Vol. 10. 1.

Supplemental Materials: High-temperature thermal diffusivity measurements using a modified Ångström's method with transient infrared thermography

Yuan Hu, Mostafa Abuseada, Abdalla Alghfeli, Saurin Holdheim, and Timothy S. Fisher
UCLA Mechanical & Aerospace Engineering Department
Los Angeles, CA USA

S1: Concentrated light source characterization

In this study the light source is controlled using an external 0-10 V programmable voltage source. In order to model the concentrated light source, we must have an expression for the total intensity as a function of the control voltage V. In this work, we heat the sample to steady state using a constant control voltage V. At steady state, the total energy absorbed from the concentrated light source and the surroundings equals energy losses via radiation,

$$q(V) + q_{surr} = q_{radiation} \tag{S1}$$

A schematic to analyze the energy balance is shown in Fig. S1A. First we calculate $q_{radiation}$. An IR image for steady-state heating is shown in Fig. S1B. We isolate the sample using a digital mask, and the processed image is shown in Fig. S1C. We compute the total radiation power by taking the summation of pixel-wise radiation using the data in Fig. S1C:

$$q_{radiation} = \Sigma_{i=1}^{N_p} \left(T(r_i)^4 \varepsilon_{front} 2\pi r_i \Delta r + T(r_i)^4 \varepsilon_{back} 2\pi r_i \Delta r \right) + 2\pi R d_z \varepsilon T(R)^4 \tag{S2}$$

where dz is the sample thickness, and $2\pi R d_z \varepsilon T(R)^4$ indicates radiation from the edge.

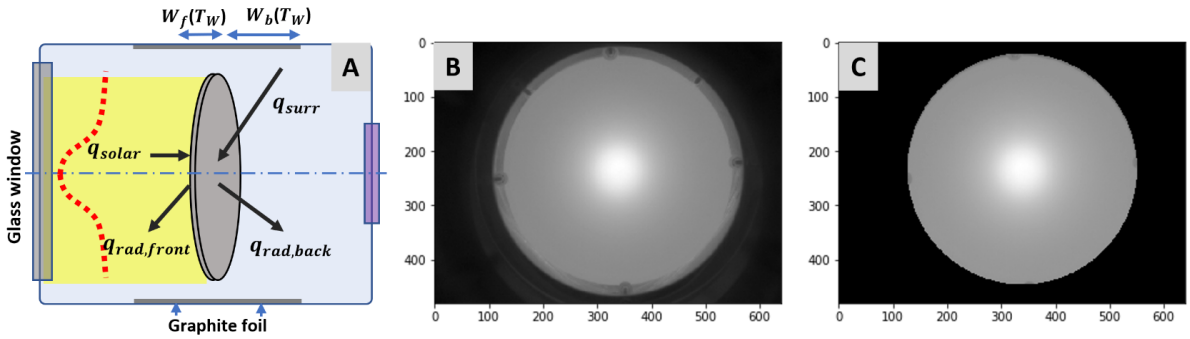

Fig. S1. (A) Schematic for solar simulator characterization. (B) An IR image of the sample. (C) An IR image with a circular digital mask to isolate the sample for radiation calculations.

In this study a layer of graphite foil with high-emissivity coating is wrapped around the sample holder to minimize stray reflection. The graphite foil's temperatures T_W on the back side were measured using the IR camera, and we assume the temperature is constant for the entire foil. The radiation from the graphite foil absorbed by the sample is calculated using:

$$q_{surr} = (A_f F_{fs} \sigma \varepsilon_{front} + A_b F_{bs} \sigma \varepsilon_{back}) T_w^4 \tag{S3}$$

where A_f and A_b are the area of the graphite foil at the front and back side. F_{fs} and F_{bs} indicates the view factor between the graphite foil to the sample at the front and back side respectively. The intensity of the concentrated light source follows a Lorentzian distribution defined in Eq. 1 in the main paper. We integrate the intensity distribution over sample's radius R and further multiply with absorptivity of the sample η to obtain the rate of energy absorbed from the light source $q(V)$:

$$q(V) = \int_0^R \frac{\eta A(V)}{\pi} \frac{\sigma_{solar}}{\sigma_{solar}^2 + r^2} 2\pi r dr = \eta A(V) \sigma_{solar} \ln \frac{R^2 + \sigma_{solar}^2}{\sigma_{solar}^2} \tag{S4}$$

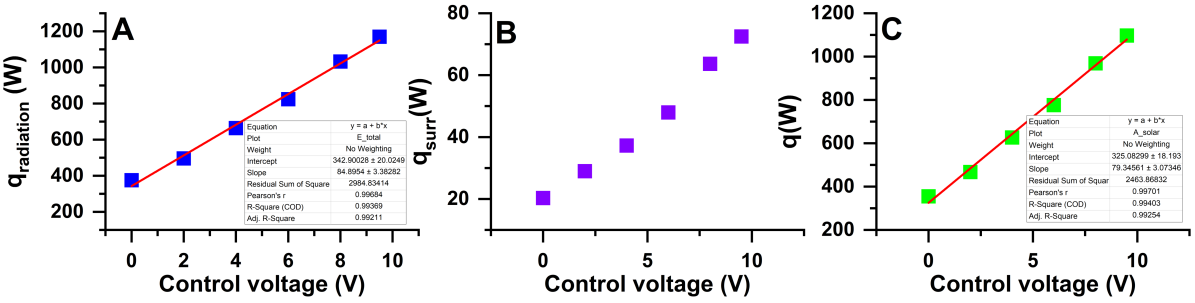

Fig. S2. (A) Total emissive power ($q_{radiation}$) of the sample measured at different control voltages. (B) Total absorption power measured from surrounding at different control voltages (q_{surr}). (C) Total energy absorbed by the sample from the concentrated light source $q(V)$ at different control voltages.

Using Eq. S1, $q(V)$ is further expressed as:

$$\begin{aligned}\eta A(V)\sigma_{solar}\ln\frac{R^2+\sigma_{solar}^2}{\sigma_{solar}^2} =& \Sigma\left(T(r_i)^4\varepsilon_{front}\,2\pi r_i\Delta r + T(r_i)^4\varepsilon_{back}\,2\pi r_i\Delta r\right)\\ &+2\pi R d_z\varepsilon T(R)^4-(A_f F_{fs}\sigma\varepsilon_{front}+A_b F_{bs}\sigma\varepsilon_{back})T_w^4\end{aligned} \tag{S5}$$

In this study, σ_{solar} is treated as a random variable and estimated using the Bayesian framework. For a specific σ_{solar}, the other parameter of the Lorentzian distribution $A(V)$ is determined using Eq. S5.

S2: Discretizing the governing equation and the Newton's solver

The governing equation of energy balance is expressed as:

$$\frac{\partial}{\partial r}\left(k\frac{\partial T}{\partial r}\right)+\frac{1}{r}\left(k\frac{\partial T}{\partial r}\right)+\frac{q_s^{''}}{dz}-\frac{(\varepsilon_{back}+C_{lb,m}/(d\theta\,r\,dr))\sigma T^4}{dz}+\frac{q_{lb,m}+q_{surr,back}}{r\,dr\,d\theta\,dz}=\rho\,c_p\frac{\partial T}{\partial t} \tag{S6}$$

The initial and the boundary conditions are:

$$\begin{cases}\text{IC: } t=0,\ T(x,0)=T_i & \text{(S7a)}\\ \text{BC: } r=R,\ -k\dfrac{\partial T}{\partial r}=\sigma(\varepsilon T^4-\eta\,T_W^4) & \text{(S7b)}\\ \text{has to satisfy: } \dfrac{\partial T}{\partial r}|_{r=0}=0 & \text{(S7c)}\end{cases}$$

Eq. S6 is discretized using the central-difference method, and thermal properties are evaluated at arithmetic mean temperature.

$$\begin{aligned}\frac{\partial}{\partial r}\left(k\frac{\partial T}{\partial r}\right)&=\frac{1}{\Delta r}\left[\left(\frac{k_{m+1}^{p-1}+k_m^{p-1}}{2}T_{m+1}^p-\frac{k_{m+1}^{p-1}+k_m^{p-1}}{2}T_m^p\right)\Delta r-\left(\frac{k_m^{p-1}+k_{m-1}^{p-1}}{2}T_m^p-\frac{k_m^{p-1}+k_{m-1}^{p-1}}{2}T_{m-1}^p\right)\Delta r\right]\\ &=\frac{1}{2\Delta r^2}\left[(k_{m+1}^{p-1}+k_m^{p-1})T_{m+1}^p-(k_{m+1}^{p-1}+2k_m^{p-1}+k_{m-1}^{p-1})T_m^p+(k_{m+1}^{p-1}+k_m^{p-1})T_{m-1}^p\right]\end{aligned} \tag{S8}$$

$$\frac{k}{r}\frac{\partial T}{\partial r}=\frac{k_m^{p-1}}{r}\frac{T_{m+1}^p-T_{m-1}^p}{2\Delta r}=\frac{k_m^{p-1}(T_{m+1}^p-T_{m-1}^p)}{2\,r\,\Delta r} \tag{S9}$$

$$\rho c_p \frac{\partial T}{\partial t} = \rho c_p \frac{T_m^p - T_m^{p-1}}{\Delta t} \tag{S10}$$

The discretized governing equation for a node m and at time step p is further expressed as:

$$T_m^{p-1} = A_m T_{m-1}^p + B_m T_m^p + C_m T_{m+1} + D_m T_m^{p4} + E_m + F_m \tag{S11}$$

where

$$A_m = -\frac{\alpha_{ba}\Delta t}{\Delta r^2} + \frac{\Delta t \alpha}{2 r \Delta r}\,,\ \alpha = \frac{k_m^{p-1}}{\rho c_m^{p-1}}\,,\ \alpha_{ba} = \frac{k_m^{p-1} + k_{m-1}^{p-1}}{2\rho c_m^{p-1}} \tag{S12}$$

$$B_m = \frac{2\Delta t}{\Delta r^2}\alpha_{ce} + 1\,,\ \alpha_{ce} = \frac{k_{m+1}^{p-1} + 2k_m^{p-1} + k_{m-1}^{p-1}}{4\rho c_m^{p-1}} \tag{S13}$$

$$C_m = -\frac{\Delta t}{\Delta r^2}\alpha_{fo} - \frac{\Delta t \alpha}{2r\Delta r}\,,\ \alpha_{fo} = \frac{k_{m+1}^{p-1} + k_m^{p-1}}{2\rho c_m^{p-1}} \tag{S14}$$

$$D_m = \frac{(C_{lb}/(2\pi r \Delta r) + \varepsilon_{back})\sigma \Delta t}{dz\,\rho\, c_m^{p-1}} \tag{S15}$$

$$E_m = -\frac{\ddot{q_s}\Delta t}{dz\,\rho\, c_m^{p-1}} \tag{S16}$$

$$F_m = -\frac{q_{lb,m} + q_{surr,back}}{r\,dr\,dz}\frac{\Delta t}{\rho c_m^{p-1}} \tag{S17}$$

For $r = 0$, the governing equation must satisfy the symmetry condition. Here we introduce a ghost node T_{-1}^p. Using central differencing, the symmetry condition is expressed as:

$$\frac{\partial T}{\partial r} = \frac{T_{-1}^p - T_1^p}{2\Delta r} \tag{S18}$$

Therefore, $T_{-1}^p = T_1^p$. The finite difference equation for the node at the center $r = 0$ is expressed as:

$$T_0^{p-1} = (A_0 + C_0)T_1^p + B_0 T_0^p + D_0 T_0^4 + E_0 + F_0 \tag{S19}$$

Consider the boundary condition at $r = R$. We introduce another ghost node outside domain T_{N+1}^p. Using central

difference method, Eq. S7b is discretized as:

$$-k_N^{p-1}\frac{T_{N+1}^p - T_{N-1}^p}{2\Delta r} = \sigma(\varepsilon T^4 - \eta T_W^4) \tag{S20}$$

The temperature at the last node is:

$$T_N^{p-1} = (A_N + C_N)T_{N-1}^p + B_N T_N^p + (D_N - \frac{2C_N\Delta r\sigma\varepsilon}{k_N^{p-1}})T_N^{p4} + E_N + F_N + \frac{2\Delta r\sigma\eta T_W^4 C_N}{k_N^{p-1}} \tag{S21}$$

The finite difference equations (Eq. S19, Eq. S11 and Eq. S21) are solved implicitly using Newton-Raphson's method. Here we denote temperatures before and after Newton-Raphson update as $T^{'}$ and T. If we define the residual using:

$$G = -T_m^{p-1} + A_m T_{m-1}^p + B_m T_m^p + C_m T_{m+1} + D_m T_m^{p4} + E_m + F_m \tag{S22}$$

Using Newton-Ralphson's method we obtain:

$$J(T^{'})(T - T^{'}) = -G(T^{'}) \tag{S23}$$

where $J(\cdot)$ indicates the Jacobian matrix for G and is shown below:

$$\begin{Bmatrix} B_0 + 4D_0T_0^{',P3}, & A_0 + C_0, & 0 & 0 & 0 & 0 & ..... \\ 0 & ... & A_m, & B_m, & C_m, & 0 & ..... \\ 0 & 0 & 0 & 0 & ... & A_N + C_N, & B_N + 4(D_N - \frac{2C_N\Delta r\sigma\varepsilon}{k_N^{p-1}})T_N^{'p3} \end{Bmatrix} \begin{bmatrix} \delta T_0 \\ \delta T_1 \\ ... \\ \delta T_N \end{bmatrix} = - \begin{bmatrix} G_0(T^{'}) \\ G_1(T^{'}) \\ ... \\ G_N(T^{'}) \end{bmatrix} \tag{S24}$$

At a given time step temperature is updated as:

$$T = T^{'} + \delta T \tag{S25}$$

For each time step the convergence criteria is $\delta T < 10^{-12}$ K.

A mesh independence study was conducted to determine the optimal number of nodes for the 1D transient heat transfer simulation. We examine the relative error in transient temperature profiles, amplitude decay, and phase shift for simulations with fewer number of nodes compared to a simulation with a high number of nodes ($N = 600$). As observed in Fig. S3, choosing $N \approx 200$ yields high accuracy (less than 0.1%) and fast computing speed (approx. 40 s compared to 5 mins with $N = 600$). In this study, we discretize the radius of the sample with approx. 220 nodes.

S3: Light blocker temperature measurement

In this study the light blocker is placed very close to the front of the sample so that the intensity of the truncated light source can be modeled with a simple window function shown in Fig. 1C. Placing thermocouples on the light blocker is difficult because of limited space. Because the light blocker facing the sample is coated with high-temperature, high-emissivity coating, we use the IR camera to measure the light blocker temperature along the radial direction by introducing a disk that is identical to samples under test but cut with a narrow slot along the radial direction. We heat this sample to identical working conditions (the same bias control voltage) and measure the temperature within the narrow slot using the IR camera. An IR image for the sample with slot is shown in Fig. S4A, and the steady temperatures measured at different radius are shown in Fig. S4B. However, because of the slot on the disk, the measured light blocker temperature differs from that without the slot. The light blocker temperature is also difficult to determine precisely because reflection from the front side of the sample (facing the solar simulator) is difficult to quantify. However, because of the high-emissivity coating on the light blocker, the error caused by unknown reflection is estimated to be less than 20 K. To mitigate these system errors, we treated the light blocker temperature $T(r)$ as a random variable and assumed it equals to the temperatures measured by

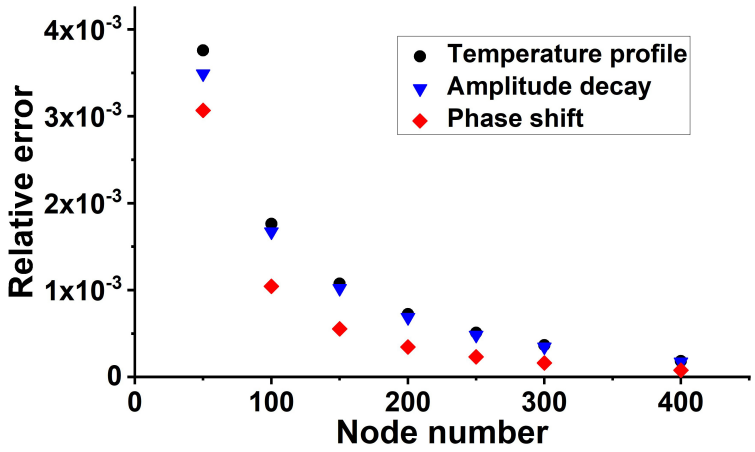

Fig. S3. Relative error in amplitude decay, phase shift and transient temperature profiles with increased number of nodes.

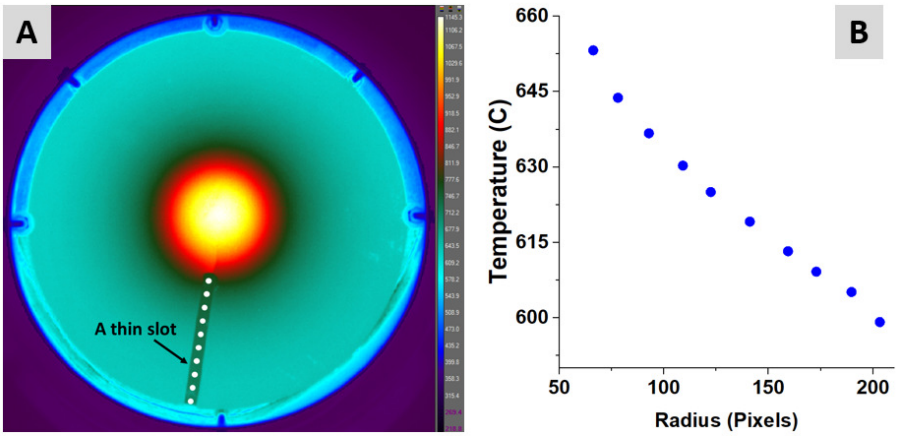

Fig. S4. (A) An IR image for a sample with a narrow slot for light blocker temperature measurements. (B) Measured light blocker temperature at different radial locations.

the IR camera $T_{IR}(r)$ plus an unknown bias temperature:

$$T(r) = T_{IR}(r) + T_{bias} \tag{S26}$$

We employ the Bayesian framework to estimate the unknown bias temperature T_{bias}.

Based on experimental observations, temperature gradients on the light blocker are low. For simplicity, we model the light blocker temperature distribution using three discrete temperatures, as demonstrated in Fig. 2B. To examine this effect, we repeated the simulation by modeling the light blocker temperature using five discrete temperatures, and the results are given below. Note that neither temperature profiles nor amplitude and phase results are affected.

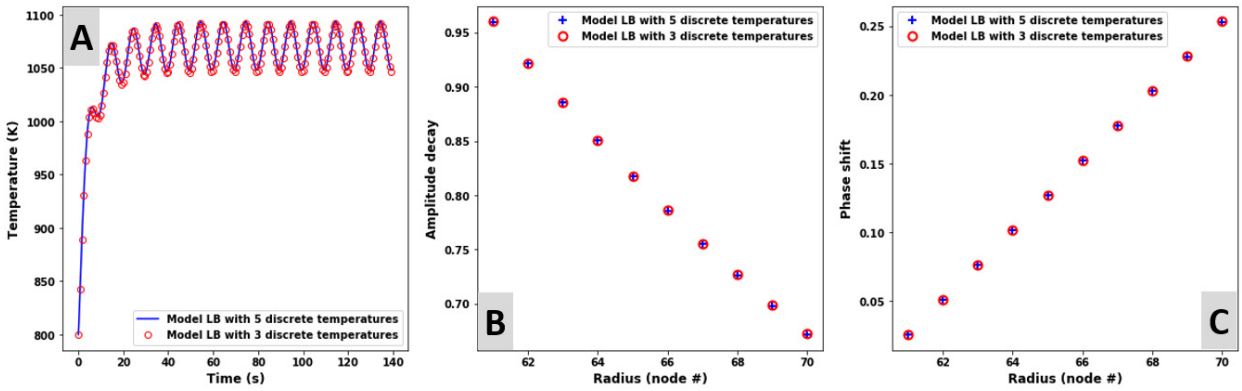

Fig. S5. (A) Temperature profile at node # 60 computed using three vs five discrete light blocker temperatures. (B) Amplitude decay and (C) phase shift results computed using three vs five discrete light blocker temperatures.

S4: Effect of random noise at high temperatures

Under extreme temperatures high noise exists, as shown in Fig. 5B. Therefore, to reduce such random noise, we average the pixels along the isothermal locations, i.e., constant radius, as shown in Fig. S6A. Our approach is to convert temperature measurements in Cartesian coordinates shown in Fig. S6A to a polar coordinates using bilinear interpolation illustrated in Fig. S6B.

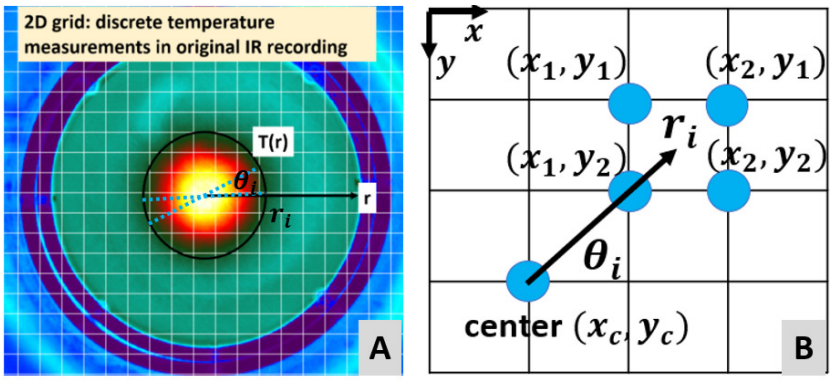

Fig. S6. (A) Temperature data in Cartesian coordinate. (B) Average Cartesian temperature data to polar coordinate using bilinear interpolation.

First we identify the center of the light source (x_c, y_c). Then for each discrete radius r_i ($r_i \in [1, 2...N]$, unit pixels), we divide it into N_{angle} evenly spaced points along the circle. To estimate the temperature of a particular point at angle θ_i, we employ bilinear interpolation using the nearest four temperatures in Cartesian coordinate using Eq. S27. We average temperatures obtained at 200 evenly spaced θ_i ranging from 0 to 2π to find the mean temperature at r_i. Then the procedure is repeated to determine all the mean temperatures along the sample's radial direction. Lastly we employ parallel computing to execute the foregoing process for all images in an IR recording. The final result is averaged radial temperatures as a function of time shown in Fig. 5C.

$$T(R,\theta) \approx \frac{y_2 - R\sin(\theta)}{y_2 - y_1} T\left(R\cos(\theta), y_1\right) + \frac{R\sin(\theta) - y_1}{y_2 - y_1} T\left(R\cos(\theta), y_2\right) \tag{S27}$$

S5: Amplitude decay and phase shift calculation

Given two quasi-steady-state oscillating temperature profiles $v_1(t)$ and $v_2(t)$. The amplitude decay ΔA and phase shift $\Delta\phi$ are calculated using a discrete Fourier transform (DFT), where $n\Delta$ indicates discrete samples.

$$dA = \left| \frac{\mathrm{DFT}(v_1(n\Delta))}{\mathrm{DFT}(v_2(n\Delta))} \right| , \; d\phi = \angle \frac{\mathrm{DFT}(v_1(n\Delta))}{\mathrm{DFT}(v_2(n\Delta))} \tag{S28}$$

For an IR image shown in Fig. S7A, we divide such an image into eight areas and analyze amplitude and phase within each area bounded by dashed blue lines and the region of interest (bounded by dashed red and black lines). The corresponding amplitude decay and phase shift results are shown in Fig. S7B and C respectively.

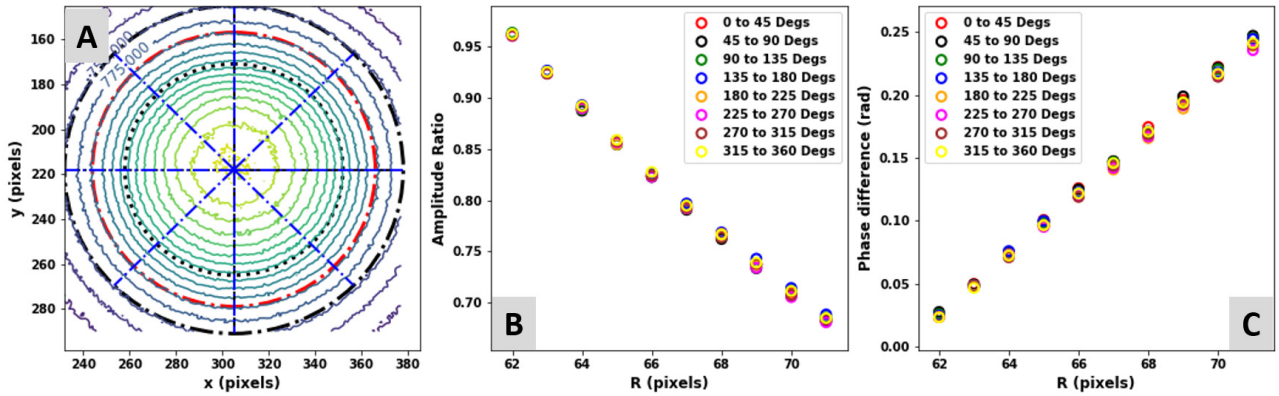

Fig. S7. (A) Temperature contour plot of an IR image. The black dots indicate the area irradiated by the concentrate light source. The region of analysis for amplitude and phase is bounded by the red and black dashed line. (B) Amplitude decay for different angular regions (shown in A) on the sample. (C) Phase shift for different angular regions (shown in A) on the sample.

S6: Results for a less conductive material: Titanium

For less conductive materials, the concentrated light source tends to cause significant thermal stress on the samples. We tested a titanium sample, which deformed quite significantly upon testing. Although the measured thermal diffusivity is reasonable compared to the reference values [42], we do not recommend testing materials with lower thermal diffusivity, *e.g.*, less than approx. 1×10^{-5} m^2/s, using the custom instrument in the temperature range considered in this work.

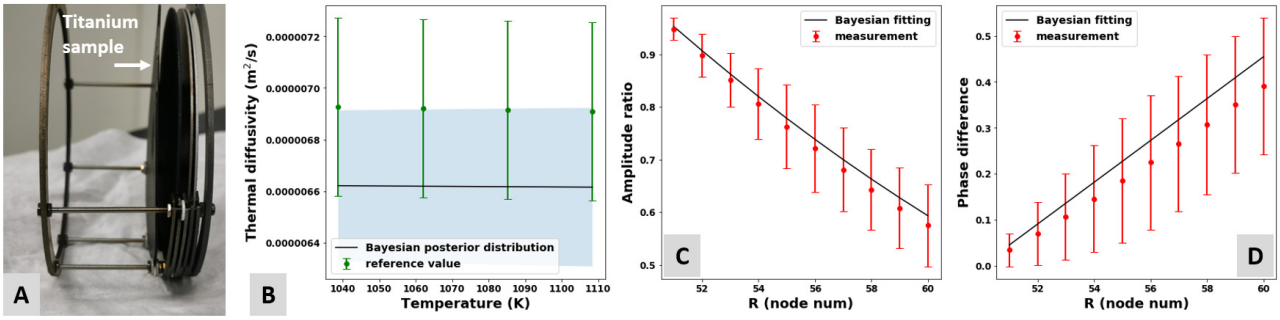

Fig. S8. (A) A photograph of the titanium sample after testing. (B) Thermal diffusivity as a function of temperature evaluated using the posterior mean of A_α and B_α (solid black line) and corresponding uncertainties (blue shade). The reference values are shown as the solid green lines [42]. Fitted (solid black lines) amplitude decay (C) and phase shift (D) within the region of analysis.